J. Fluid Mech. (1997), *vol.* 332, *pp.* 185–214

Coherent structures near the wall in a turbulent channel flow

By J. JEONG[1], F. HUSSAIN[1], W. SCHOPPA[1] AND J. KIM[2]

[1]Department of Mechanical Engineering, University of Houston,
Houston, TX 77204-4792, USA

[2]Mechanical and Aerospace Engineering Department, University of California Los Angeles,
Los Angeles, CA 90095-1597, USA

(Received 14 August 1995 and in revised form 27 August 1996)

Coherent structures (CS) near the wall (i.e. $y^+ \leqslant 60$) in a numerically simulated turbulent channel flow are educed using a conditional sampling scheme which extracts the entire extent of dominant vortical structures. Such structures are detected from the instantaneous flow field using our newly developed vortex definition (Jeong & Hussain 1995) – a region of negative λ_2, the second largest eigenvalue of the tensor $S_{ik}S_{kj} + \Omega_{ik}\Omega_{kj}$ – which accurately captures the structure details (unlike velocity-, vorticity- or pressure-based eduction). Extensive testing has shown that λ_2 correctly captures vortical structures, even in the presence of the strong shear occurring near the wall of a boundary layer. We have shown that the dominant near-wall educed (i.e. ensemble averaged after proper alignment) CS are highly elongated quasi-streamwise vortices; the CS are inclined 9° in the vertical (x, y)-plane and tilted ±4° in the horizontal (x, z)-plane. The vortices of alternating sign overlap in x as a staggered array; there is no indication near the wall of hairpin vortices, not only in the educed data but also in instantaneous fields. Our model of the CS array reproduces nearly all experimentally observed events reported in the literature, such as VITA, Reynolds stress distribution, wall pressure variation, elongated low-speed streaks, spanwise shear, etc. In particular, a phase difference (in space) between streamwise and normal velocity fluctuations created by CS advection causes Q4 ('sweep') events to dominate Q2 ('ejection') and also creates counter-gradient Reynolds stresses (such as Q1 and Q3 events) above and below the CS. We also show that these effects are adequately modelled by half of a Batchelor's dipole embedded in (and decoupled from) a background shear $U(y)$. The CS tilting (in the (x, z)-plane) is found to be responsible for sustaining CS through redistribution of streamwise turbulent kinetic energy to normal and spanwise components via coherent pressure–strain effects.

1. Introduction

During the past three decades, numerous types of coherent structures (CS) have been proposed to explain experimentally observed phenomena – notably, the celebrated 'bursting' process – in turbulent boundary layers. The so-called 'bursting' is responsible for most turbulence production near the wall and thus increased turbulent drag and mixing, making it the most dynamically significant event. Primarily because of its pervasive technological relevance, the turbulent boundary layer has been studied exhaustively, employing experimental, theoretical and numerical tools; yet this prototypical flow is far from being adequately understood. The review articles, let alone research papers, on this topic are far too numerous to be cited; we mention only two examples: Cantwell (1981) and Robinson (1991). Considering ‘bursting’ alone, there is yet no consensus on the associated CS. The various boundary layer CS proposed to date differ not only in their geometry, strength, and orientation, but also in their dynamical roles; further, there is also no consensus on their evolutionary dynamics. Why an adequate description of boundary layer CS is so difficult is captured well by Fiedler (1988): “Thus, when studying the literature on boundary layers, one is soon lost in a zoo of structures, e.g. horseshoe- and hairpin-eddies, pancake- and surfboard-eddies, typical eddies, vortex rings, mushroom-eddies, arrowhead-eddies, *etc* …”. While several types of CS may in fact exist in the outer region of turbulent boundary layers, it appears that the buffer region is dominated by elongated quasi-streamwise structures. The primary objective of our study is to identify and delineate the geometrical and dynamical details of dominant, near-wall CS as well as to interpret, by using tractable vortex dynamics arguments, the significant events recorded in previous conditional averaging studies. A salient feature of our study is the eduction (i.e. by ensemble averaging after appropriate relative alignment) of the three-dimensional field of the underlying CS from numerous realizations so that a generic model (not necessarily identical to any instantaneous event which consists of coherent and incoherent motions) is deduced to elucidate the dynamics in the turbulent boundary layer (Jeong & Hussain 1992; Hussain 1986).

Flow visualization studies of turbulent boundary layers provide evidence that observed bursting events are recurrent features near the wall (Kline *et al.* 1967; Corino & Brodkey 1969). Willmarth & Lu (1972) showed experimentally that most Reynolds stress production occurs during bursting, and a number of conditional averaging techniques have been developed to capture this phenomenon. The Q2 (Quadrant 2), Q4 (Quadrant 4) (Willmarth & Lu 1972) and VITA (Variable Interval Time Average; Blackwelder & Kaplan 1976) eduction schemes are the more popular ones. From VITA and quadrant analysis of Reynolds stress, Blackwelder & Eckelman (1979) suggested that counter-rotating streamwise vortices (separated in the spanwise direction) with a streamwise length of 1000 wall units are dominant. It is important to note that eduction based upon the velocity signal is unable to reveal the spatial details of the underlying CS due to the inherent smearing, making accurate analysis of CS kinematics and dynamics impossible. Studies by Townsend (1979) and Mumford (1982) are notable for capturing qualitative features of two-dimensional cuts (in the x, y-plane) of CS, leaving the three-dimensional geometry and the dynamics rather obscure. Building on the approach used in these two studies, Stretch (1989) used a template matching technique based on known trial patterns of velocity and vorticity to educe CS in a turbulent channel flow; wall-attached vortices extending to the outer region (channel centreline) were conjectured to be dominant. The above conditional averaging studies are rather inconclusive regarding CS since they did not directly extract vortical structures, shown in this paper to be crucial to the near-wall dynamics. This study is consistent with our longstanding concepts of CS as dynamically significant, large-scale flow regions of instantaneously correlated vorticity fluctuations (Hussain 1980, 1983*a*). The goal here is to record the features of the underlying (i.e. educed) CS which capture the dominant three-dimensional dynamical events in the boundary layer by flow decomposition into coherent and incoherent parts and thus to produce a conceptual model. This approach is a continuation of our efforts in free shear flows (e.g. Hussain & Zaman 1980; Husain & Hussain 1993).

Using instantaneous isopressure surfaces obtained from a numerically simulated boundary layer (Spalart 1988), Robinson (1991) showed that quasi-streamwise structures are in fact prominent near the wall. Since his study focused on instantaneous events, ensemble-averaged CS and their dynamics were not addressed. Although the presence of streamwise vortices in near-wall turbulence is now commonly accepted, their evolutionary dynamics remain an unresolved issue. A notable initiative in this regard was that of Jimenez & Moin (1991), who studied channel flow in a minimal domain size for sustained turbulence. In this way, the evolution of a minimal periodic flow unit containing at most two near-wall streamwise vortices was tracked in space and time. In a related study with an even simpler configuration – minimal Couette flow – Hamilton, Kim & Waleffe (1995) identified an underlying quasi-cyclic regeneration process.

In this paper, our primary objective is to study the spatial relation of near-wall CS with experimentally observed events during the so-called ‘bursting’ process. We are not interested in the details of individual events but in coherent (i.e. ensemble-averaged), thus statistically significant, structural properties. Although the educed CS cannot fully explain the evolutionary dynamics (in the absence of forcing), strong dynamical inferences can be made, as shown here. Furthermore, all of the instantaneous kinematic features near the wall classified by Robinson (1991) are captured in a single ensemble-averaged flow field, reported in our paper. Our general-purpose eduction scheme (an extension of the algorithm developed by Hussain & Hayakawa 1987 for structure eduction in a turbulent cylinder wake) extracts three-dimensional structures from the instantaneous near-wall flow – where vortical structures cannot be detected simply by vorticity magnitude – by utilizing our new definition of a vortex.

Experimental acquisition of instantaneous velocity and vorticity field data of three-dimensional flows is currently impossible due to limitations of measurement technology (the reason why our generic eduction scheme was previously limited to two-dimensional cuts of vorticity fields of three-dimensional structures; see Hussain & Hayakawa 1987 and Hayakawa 1992). Thus, we use a well-resolved numerical simulation database of turbulent channel flow (Kim, Moin & Moser 1987) to educe fully three-dimensional CS. Using this database, we previously educed spanwise structures in the outer region (Hussain, Jeong & Kim 1987). Here, we study CS in the buffer region since most turbulence production occurs here and, most importantly, because these CS are the ones that matter in drag and heat and mass transfer.

Based on the ensemble-averaged vortical structure, we will associate its spatial configuration with experimentally observed events such as VITA, quadrant Reynolds stresses (Q1, Q2, Q3 and Q4), and spanwise inflection of streamwise velocity profiles $u(z)$. Using an inviscid model of CS, we will demonstrate how negative and positive Reynolds stress events arise due to cross-stream advection and also explain why Q4 events dominate Q2 near the wall. In addition, an intercomponent (among different physical directions) energy transfer scenario will be discussed, which is of particular importance for near-wall turbulence modelling and for development of boundary layer control techniques.

In the next section, we analyse instantaneous flow fields to evaluate characteristic features of CS in the buffer region. In §3, our eduction scheme is described along with its advantages compared with those of previous studies. From the educed data, a conceptual model for CS showing its spatial relationship with VITA, Q2, and Q4 events are discussed in §4. We also analyse the phase difference between u and v fluctuations induced by near-wall CS and the resulting effect on the Reynolds stress. In addition, we consider the role of CS on the near-wall vortex line geometry, intercomponent energy transfer, and the wall pressure distribution.

2. Instantaneous flow field

The numerical simulation database to be analysed consists of turbulent channel flow at the Reynolds number, $Re = U_c h/\nu \approx 3300$ (Kim *et al.* 1987), where U_c is the centreline velocity and h is the channel half-width. Kim *et al.* have validated this database by comparison with numerous independent experimental and numerical studies. Throughout this paper, $x(u)$, $y(v)$ and $z(w)$ denote the streamwise, wall-normal, and spanwise directions (velocities) respectively. Velocity, length, and time are normalized in wall units as $u^+ = u/u^* \equiv u/(\tau_w/\rho)^{1/2}$, $l^+ = lu^*/\nu$, $t^+ = tu^{*2}/\nu$, where τ_w, ρ and ν denote wall-shear stress, density, and kinematic viscosity. Wall units are used throughout the paper, unless mentioned otherwise. The grid sizes in the streamwise and spanwise directions are 17.7 and 5.9 wall units, with variation in the normal direction from 0.05 near the wall to 4.4 due to the use of cos mapping for Chebyshev polynomial expansion.

To educe CS and study their dynamics, we must first develop a means to extract vortex cores directly from the instantaneous velocity field. For this purpose, the vorticity magnitude is a poor choice, since high vorticity magnitude is present everywhere near the wall, due to the background shear. We have found that such vortices buried within a vorticity layer are well-represented by connected regions where the second largest eigenvalue (λ_2) of the tensor $S_{ik}S_{kj} + \Omega_{ik}\Omega_{kj}$ is negative (see Jeong & Hussain 1995); here $S_{ij} \equiv (u_{i,j} + u_{j,i})/2$ and $\Omega_{ij} \equiv (u_{i,j} - u_{j,i})/2$ are the symmetric and antisymmetric parts of the velocity gradient tensor $u_{i,j} \equiv \partial u_i/\partial x_j$. This definition has been validated for a variety of vortical flows, including both DNS data and analytical solutions, even in situations when both intuitive and other recent definitions (e.g. Hunt, Wray & Moin 1988; Chong, Perry & Cantwell 1990) may not hold. Unlike $|\boldsymbol{\omega}|$, which works well in free shear flows, this definition correctly identifies a streamwise vortex embedded in a homogeneous shear flow – a model which qualitatively resembles quasi-streamwise vortices near the wall. As will be seen, an important advantage of this identification scheme is that it is not constrained to preferentially detect organized events with a certain orientation, such as techniques based on velocity vectors in (y, z)-planes (Bernard, Thomas & Handler 1993) or streamwise vorticity (Jimenez & Moin 1991).

Before considering instantaneous fields, we first show some statistics associated with the new vortex definition to identify the preferred location and orientation of vortical structures – information necessary for eduction. It is important to note that λ_2 is positive everywhere outside vortex cores, especially near stagnation regions, where the positive λ_2 magnitude is comparable to the $-\lambda_2$ values within vortices. For example, in figure 1(*a*), $\overline{\lambda_2}$ is positive for $y^+ < 10$ and also comparable to λ_2', reflecting that the viscous sublayer contains no vortices (primes denote root-mean-square values). The fact that $\overline{\lambda_2}$ is much smaller than λ_2' in figure 1(*a*) for $10 < y^+ < 30$ indicates substantial cancellation of positive (stagnation) and negative (vortex core) regions of λ_2 in a spatial mean within the buffer region; the negative value of $\overline{\lambda_2}$ only suggests that vortices are slightly more common. Thus, λ_2' is more effective than $\overline{\lambda_2}$ as a statistical indicator of vortical events. In figure 1(*a*), the peak of $\lambda_2'(y)$ is located at $y^+ \approx 23$, suggesting the prominence of vortical structures in the buffer region. The large values of λ_2' at higher y indicate the presence of outer-scale vortices, which will not be considered here. For comparison, vorticity component and pressure fluctuation statistics (non-dimensionalized by u^{*2}/ν and ρu^{*2}) are shown in figure 1(*b*).

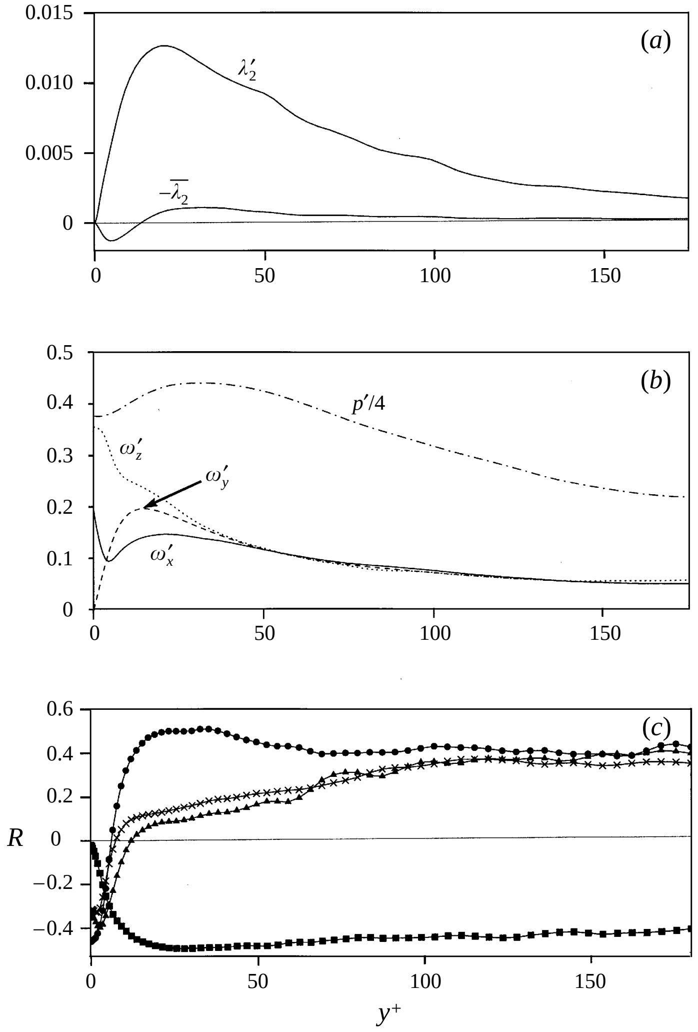

FIGURE 1. (*a*) Mean and r.m.s. profiles of $-\lambda_2$; (*b*) profiles of r.m.s. vorticity components ω_x', ω_y', ω_z' and pressure p'; (*c*) cross-correlation of $-\lambda_2$ with: •, $|\omega_x|$; ×, $|\omega_y|$; △, $|\omega_z|$; and ■ pressure fluctuation.

From a structural standpoint, these statistics reflect some important features of both instantaneous and our educed flow fields. In particular, ω_x' has two peaks: one in the buffer layer due to the streamwise vortices studied here and another at the wall resulting from the opposite-signed ω_x present underneath vortices, created by the no-slip condition at the wall. Near the wall, ω_z' is high due to the presence of low- and high-speed streaks, which cause strong z-variation of $u(y)$ and hence ω_z. The fact that ω_y' peaks at lower y than the second peak of ω_x' is consistent with the ensemble-average CS data presented in §4.4.

To determine the dominant CS orientation, we computed cross-correlation coefficients (note that all correlations discussed in the following are normalized correlation coefficients) of $-\lambda_2$ with each component of vorticity (figure 1*c*). Near the wall ($10 < y^+ < 40$), the cross-correlation between $-\lambda_2$ and $|\omega_x|$ is much higher than that between $-\lambda_2$ and $|\omega_y|$ or $|\omega_z|$; thus, the structures are nearly aligned in the streamwise direction. The strong negative correlation of each vorticity component magnitude with

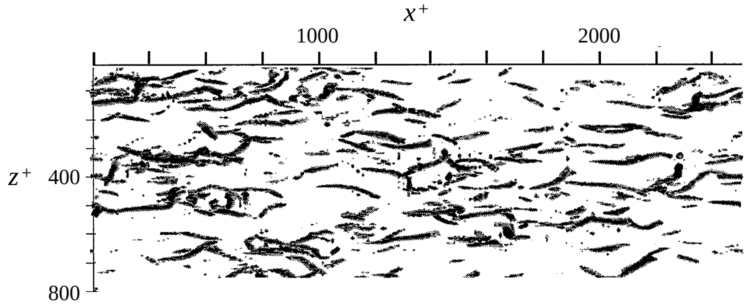

FIGURE 2. Top view of the isosurfaces of $\lambda_2 = -0.03$ in the range $0 < y^+ < 60$.

$-\lambda_2$ in the viscous sublayer implies that large vorticity here is not associated with vortices, as discussed above. The poor correlation between pressure fluctuations and $-\lambda_2$ in the viscous sublayer is presumably due to the fact that λ_2 is predominantly positive here while the pressure footprint from vortices everywhere contains both positive and negative regions (discussed later), resulting in a small cross-correlation. The correlations between $-\lambda_2$ and each vorticity component become equal to one another as y approaches the centreline of the channel, implying that the structures in the outer region have no preferred direction (i.e. isotropic vorticity fluctuations), unlike the streamwise orientation of near-wall vortices; the equality of ω'_x, ω'_y and ω'_z in the outer region shown in figure 1(*b*) is also consistent with isotropy. Above the viscous sublayer, the cross-correlation between $-\lambda_2$ and pressure is observed to be as high as that between $|\omega_x|$ and $-\lambda_2$, suggesting that CS identified by $-\lambda_2$ also contain regions of low pressure; this is consistent with the definition of λ_2, which is based on the Hessian of pressure. However, as shown in the following, the inverse is not true: i.e. not all regions of low pressure are included in the λ_2-based vortex definition.

The top view of an isosurface of $\lambda_2 = -0.03$ in the range $0 < y^+ < 60$ of a representative instantaneous field reveals a large collection of slender near-wall structures (figure 2). Clearly, the dominant vortices are in fact aligned predominantly with x, with a streamwise extent of about 200 wall units. Note the absence, let alone preponderance, of individual vortices having streamwise length of 1000 wall units (comparable to the length of low-speed streaks) suggested by Blackwelder & Eckelman (1979). The observed quasi-streamwise vortices appear to overlap along their streamwise extent, indicating the importance of their mutual interaction (addressed in §4). The total length of a chain of these overlapping vortices can be as large as 800 wall units. In this range of y, no hairpin-type structures are apparent; our educed data in §4 also indicate that hairpin vortical structures are very rare.

By comparing isosurfaces of positive and negative ω_x (figure 3*a*, *b*) with those of negative λ_2 (figure 2), we observe that there exists a one-to-one correspondence between regions of large $-\lambda_2$ and $|\omega_x|$. It should be emphasized that ω_x regions (with an opposite sign to that of the structure) appear below each vortex immediately next to the wall, as expected from the no-slip condition at the wall. Thus, ω_x in the region $0 < y^+ < 10$ is not plotted in figure 3(*a*, *b*). Note that the regions with high positive (negative) ω_x tend to tilt at a positive (negative) angle with respect to the x-direction; the 'tilting' and 'inclination' angles are defined in figure 4. This dependence of the tilt angle on the sign of structure circulation appears to result from interactions between neighbouring quasi-streamwise structures, as discussed in §4.1.

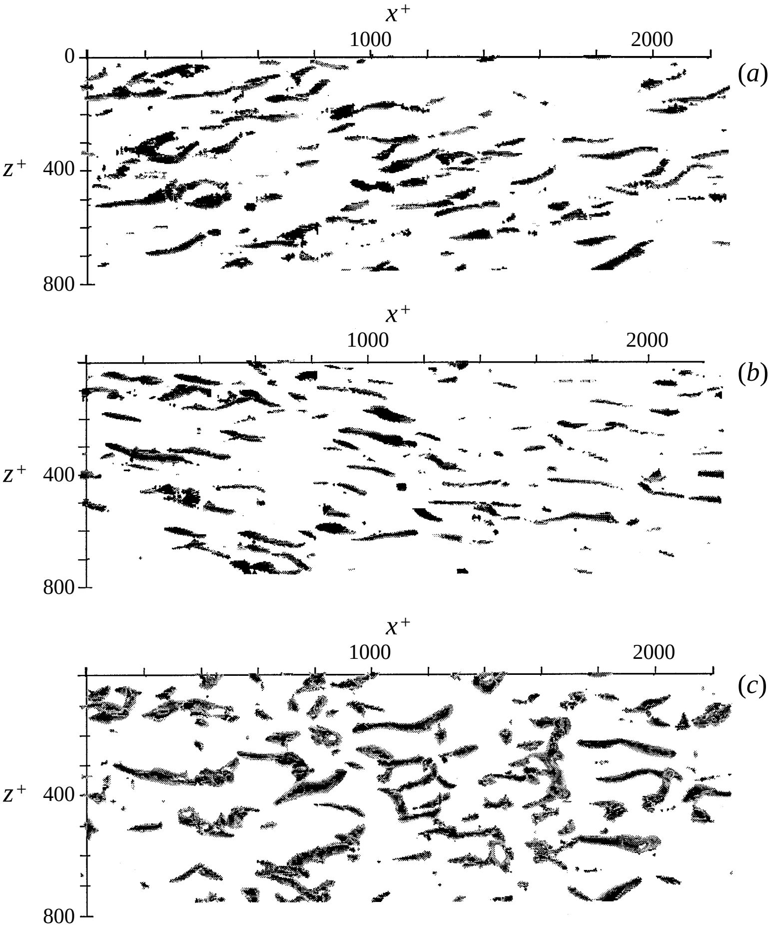

FIGURE 3. Top views of isosurfaces of: (*a*) $\omega_x = 0.3$ and (*b*) $\omega_x = -0.3$ both in the range $10 < y^+ < 60$; (*c*) $p = -0.2$ in the range $0 < y^+ < 60$.

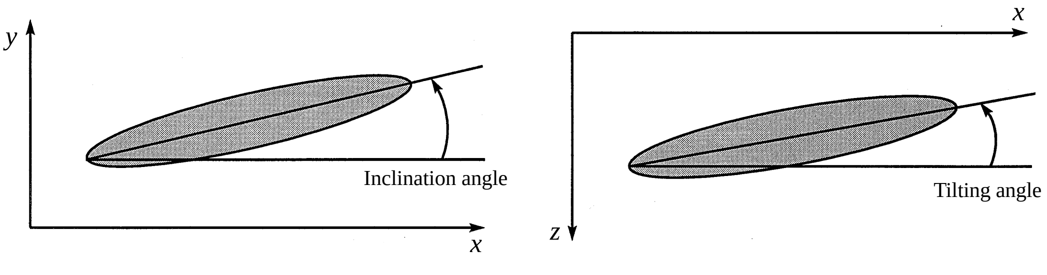

FIGURE 4. Schematics for the definitions of inclination and tilting angles.

Comparison of figures 2 and 3(*c*) shows that most λ_2 regions do in fact occur within low-pressure regions. On the other hand, there are several regions with low pressure (especially spanwise-aligned; see, for example $(x^+, z^+) \approx (780,350), (800,600)$ and $(1700,300)$) which do not correspond to regions of negative λ_2. This is due to the fact that the spatial scale of pressure is much larger than that of λ_2, i.e. pressure has a long-range effect in space, determined by $\nabla^2 p = -\rho(S_{ij}S_{ji} + \Omega_{ij}\Omega_{ji}) = \rho(\lambda_1 + \lambda_2 + \lambda_3)$, where $\lambda_1 \geqslant \lambda_2 \geqslant \lambda_3$ are the eigenvalues of $S_{ik}S_{kj} + \Omega_{ik}\Omega_{kj}$. As a result, pressure isosurfaces in the buffer region can reflect low-pressure contributions from large-scale, outer-region structures (whose λ_2 is localized within the vortex core and will not show up in the buffer region), resulting in many false indications of near-wall vortices by pressure isosurfaces, as illustrated above; this is also evidenced in §4.6 by the difference between the distributions of two-point correlation of wall pressure and coherent wall pressure in the ensemble-averaged field. That is, while vortical structures have low pressure, the inverse is not true. The joint p.d.f.s between pressure and ω_x also support this result (see Kim 1989).

3. Eduction scheme

Previous conditional-average studies employing VITA, Q2 and Q4 conditional samplings used velocity signals for CS eduction. Since the induced velocity of CS decays more slowly than vorticity with distance, the educed structures in those studies are expected to be more smeared than CS obtained using λ_2- or vorticity-based eduction. For the same reason, identification of the entire extent of CS using the velocity signal is difficult because a sharp structure boundary cannot be defined in the velocity field. Hence, it is difficult (if not impossible) to decipher the detailed features of the underlying vortical structure from conditional sampling (or eddy estimation) techniques employing the velocity field. Furthermore, criteria based on local velocity information may detect different parts of the same CS or even different CS types. Consequently, the educed structure can be severely smeared due to averaging of different structure types or false alignment of different features of the same structure. In fact, symmetric VITA ensemble averages can be obtained even when asymmetric VITA events are much more common in the instantaneous field (Johansson, Alfredsson & Kim 1991). Clearly, a more appropriate indicator of near-wall vortical events is required for effective CS eduction. For this purpose, we use a multi-point, λ_2 field-based scheme to educe the entire extent of vortical structures from the instantaneous flow field. Our eduction is designed to eliminate ambiguities such as multiple detections of one structure, detection of different parts of different structures, and detection of different types of structures, in order to reveal the relative spatial locations of CS and their underlying link to well-known events such as VITA, Q2 and Q4.

In this study, we educe only the quasi-streamwise structures near the wall (discussed in §2). For this purpose, we extend the vorticity-based eduction scheme used by Hussain (1986) and Hussain & Hayakawa (1987) in two ways. First, we use negative λ_2 to detect structures instead of vorticity magnitude $|\boldsymbol{\omega}|$, because, as mentioned earlier, $|\boldsymbol{\omega}|$ is high near the wall irrespective of the presence of structures. A second difference is that we consider a fully three-dimensional ensemble average, rather than planar slices of three-dimensional structures.

The basic steps in our eduction scheme are (i) to detect quasi-streamwise vortical structures containing negative λ_2 (either positive or negative ω_x) directly from the three-dimensional instantaneous flow field (note that negative λ_2 is used to identify vortical structures, while ω_x is used to distinguish between structures with different senses of rotation), (ii) to ensemble average the accepted structures of the same sense of rotation by aligning the mid-point of their streamwise extent, and (iii) to shift the alignment point to maximize cross-correlation between each realization and the ensemble-averaged field.

To find the centres of quasi-streamwise structures with positive ω_x in (y,z)-planes, we first detected local maxima of $-\lambda_2$ ($|\lambda_2| > \lambda_2'$ and positive ω_x) over $0 < y^+ < 40$ in

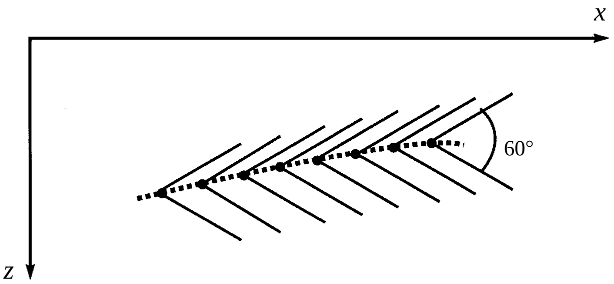

FIGURE 5. Schematic for the detection of the quasi-streamwise structure. The dots represent the locations of local maximum of $-\lambda_2$ and the solid lines denote cones at ±30°; the thick dashed line represents the vortex axis.

each (y, z)-plane. A line connecting local maxima of $-\lambda_2$ in successive (y, z)-planes was considered to be the vortex axis. Note that for all accepted realizations, regions with $|\lambda_2| > \lambda_2'$ had only one peak in each (y, z)-plane (this peak defined as the vortex axis). Each vortex was then required to satisfy the following additional two criteria: (*a*) a streamwise length of at least 150 wall units in the range $10 < y^+ < 40$ (this condition is designed to capture fully developed CS since the predominant x-lengthscale of well-defined structures in the instantaneous λ_2 field shown in figure 2 is about 200); (*b*) inclination and tilting angles (defined in figure 4) of the vortex with respect to the streamwise direction within ±30°. Condition (*b*), shown in figure 2 to be quite appropriate, is implemented by imposing cones at the structure centre in each (x, z)-plane as shown in figure 5. If a local maximum in a (y, z)-plane is contained within the cone starting at a local maximum in the adjacent upstream (y, z)-plane, the two local maxima are considered to belong to the same quasi-streamwise structure. Thus, the line containing local maxima (dashed in figure 5) represents the axis of a quasi-streamwise structure. Since this vortex tracing algorithm marches with very small steps in x ($\Delta x^+ \approx 18$), adjacent vortices would have to be virtually fused together to show up within a single cone. Such a vortex geometry has not been observed and is unlikely; thus, our technique is effective in capturing individual vortices. Note that we did not preferentially choose structures tilted in one direction. The *zeroth ensemble average* is obtained after aligning realizations at the x-centrepoint of the vortex axis.

The alignment points of the zeroth ensemble average were then shifted in both x and z to the locations that gave maximum cross-correlation between each realization and the ensemble-averaged field. The cross-correlations were computed over a three-dimensional window of $150 \times 60 \times 40$ wall units in x^+, y^+ and z^+. The shifting of alignment points was iterated until convergence in the ensemble average was reached. Any realization requiring an excessive shift (more than two grid points in x^+ or z^+) or having a small cross-correlation coefficient (below 0.4) were discarded. The ensemble average after these iterations will be called E1 in the following. The detection point (i.e. the x-centrepoint of the structure axis) is considered to be the origin ($x = 0$), $\langle . \rangle$ denotes the ensemble average, and the subscript r denotes an incoherent quantity, i.e. the deviation of each realization from the ensemble average. In E1, we obtained 104 realizations with positive ω_x using seven different instantaneous, fully developed turbulent flow fields that were separated equally by 30 wall time units.

One measure of the educed CS's frequency of occurrence in the instantaneous field is the total area occupied by it. The realizations considered here cover about 15% (number of realizations × CS area / total area) of the (x, z) projection; note that

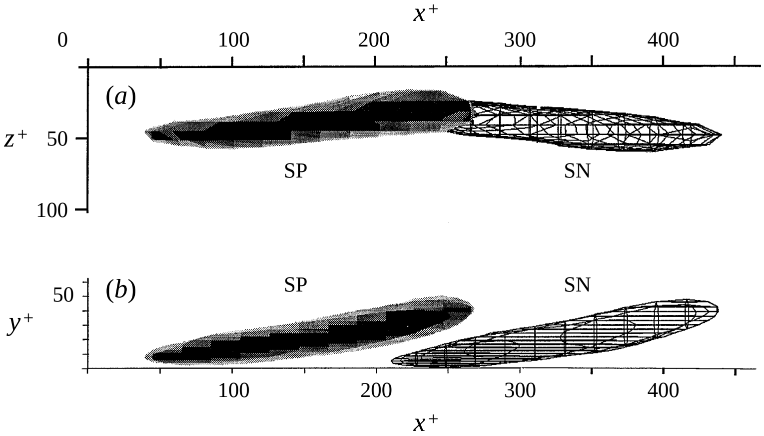

FIGURE 6. Contour plot for $\lambda_2(\partial\langle u_i\rangle/\partial x_j)$ of SP and SN in (a) top view; (b) side view. The shaded and wire frame surfaces represent SP and SN respectively. These structures are superimposed to show their relative locations and orientations.

positive and negative ω_x are equally probable. Since the educed CS and streamwise vortical events in the instantaneous flow are of comparable size, this implies that the CS is in fact a prominent feature of the instantaneous field as well (cf. flow area occupied by instantaneous vortices in figure 2).

4. Results and discussion

Since quasi-streamwise structures with positive ω_x (hereinafter called SP) are the symmetric counterparts of structures with negative ω_x (hereinafter called SN), we focus our discussion on one only, SP, except when indicated otherwise. The isosurface of $-\lambda_2(\partial\langle u_i\rangle/\partial x_j)$ for SP, from the ensemble-averaged velocity gradient tensor, shows a quasi-streamwise vortex with an inclination angle of about 9° in the vertical plane and a tilting angle of 4° in the horizontal plane (figure 6a, b). Note that $\partial\langle u_i\rangle/\partial x_j$ is denoted as the argument of λ_2 because it is obtained from the ensemble-averaged field, not ensemble averaged after being obtained from the instantaneous field; this distinction is important since $\langle\lambda_2(\partial u_i/\partial x_j)\rangle \neq \lambda_2(\partial\langle u_i\rangle/\partial x_j)$. The spatial relation between SP and SN in figure 6 was inferred from $\langle\omega_x\rangle$ and two-point correlation data, discussed below. The educed structure has a streamwise extent of 200 wall units and a diameter of 25 wall units. The vortex Reynolds number (Γ/ν) of SP is approximately 200, as compared with the average value of 140 for streamwise vortices identified by spiral streamlines in (y, z)-planes in a higher-*Re* turbulent boundary layer (Kline & Robinson 1989); $Re_\theta = 280$ for the channel flow but 1410 for the boundary layer.

The inclination angle of the educed CS agrees well with that obtained from the two-point correlation $R(\Delta x, y; y_{ref} = 20)$ of ω_x (figure 7a). The correlation $R(y, \Delta z; y_{ref} = 20)$ of ω_x (figure 7b) does not show negative regions along the span; thus, vortices near the wall do not appear in pairs along z, as would be the case if hairpin vortices were prominent. Note that hairpin vortex line bundles do occur, but should not be confused with hairpin vortices. The negative correlation near the wall seen in figure 7(a, b) is due to opposite-signed ω_x induced by the CS as a result of the no-slip condition at the wall. The negative cross-correlation at $y^+ > 30$ in figure 7(a, b) suggests that SP and SN overlap each other in x, as depicted in figure 6.

In spite of the tilting shown in the ensemble-averaged structure, the two-point

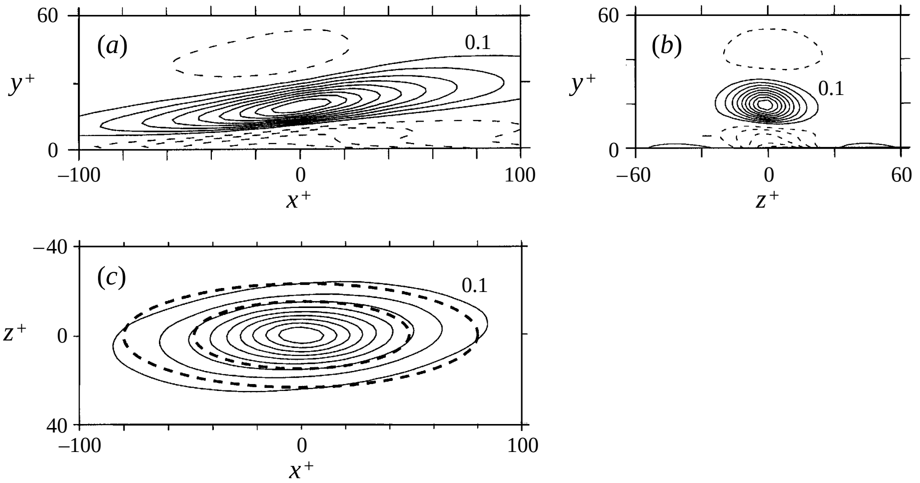

FIGURE 7. Two-point correlation coefficient of ω_x: (*a*) $R_{\omega_x\omega_x}(\Delta x, y; y_{ref} = 20)$; (*b*) $R_{\omega_x\omega_x}(y, \Delta z; y_{ref} = 20)$; (*c*) $R_{\omega_x\omega_x}(\Delta x, \Delta z; y_{ref} = 20)$. Contour spacing = 0.1; in (*c*), dashed and solid lines represent the unconditional and conditional correlations.

unconditional correlation of ω_x in an (x, z)-plane (dashed lines in figure 7*c*) is symmetric; however, this does not imply that the tilting angles of SN and SP are individually zero, but that the contributions of SN and SP to the tilt angle of the correlation contours are equal and opposite. To recover the tilting angle of the structure from a two-point correlation of ω_x, we reflect the ω_x distribution about an (x, y)-plane at the reference location whenever ω_x at this location is negative; i.e. we define an asymmetric correlation as

$$R(\Delta x, \Delta z; y_{ref} = 20) = \int \omega_x(x, z; y_{ref})\omega_x(x + \Delta x, z + i\Delta z; y_{ref})\mathrm{d}x\mathrm{d}z,$$

where

$$i = \begin{cases} 1 & \text{for } \omega_x(x, z; y_{ref}) \geqslant 0; \\ -1 & \text{for } \omega_x(x, z; y_{ref}) < 0. \end{cases}$$

The solid contours in figure 7(*c*) show the asymmetric correlation of ω_x, and the tilting angle of these contours is consistent with that of the ensemble-averaged structure (figure 6*a*). Even though the tilting and inclination angles of the educed CS are small, it will be shown in §§4.1, 4.2 and 4.7 that this slightly skewed geometry is crucial in generating the VITA events observed in various experiments and numerical simulations, and also in sustaining of CS through pressure–strain effects.

Contours of $-\lambda_2(\partial\langle u_i\rangle/\partial x_j)$ in the plane $x = 0$ (figure 8*a*) show a nearly circular core geometry with negative λ_2, surrounded by regions of non-negligible positive λ_2 (not part of the vortex core) as shown in figure 8(*b*); the fact that positive λ_2 survives in the ensemble average justifies our earlier contention that λ_2' is more appropriate than $-\overline{\lambda}_2$ as a statistical indicator of vortical events. In several contour plots which follow, we draw thick lines at two significant levels of $-\lambda_2(\partial\langle u_i\rangle/\partial x_j)$ to identify the relative spatial location of the CS. To address the interaction of SP and SN, it is necessary to first verify their spatial arrangement shown in figure 6. Unfortunately, this is not possible in ensemble average E1 because alignment at the structure mid-point causes substantial smearing of its upstream and downstream ends. Note that the 'ends' of a given vortical event are precisely defined by our eduction procedure

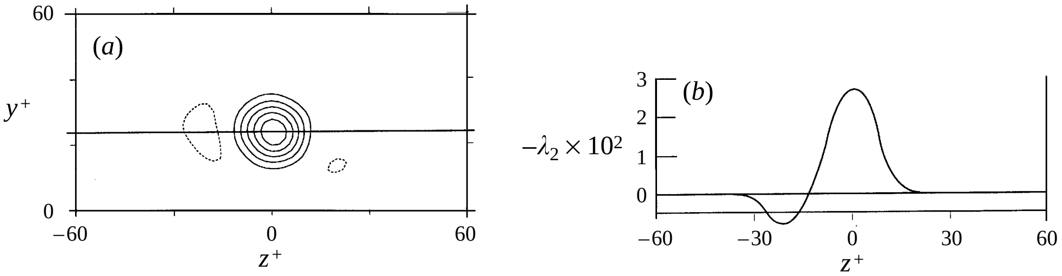

FIGURE 8. (*a*) $\langle -\lambda_2 \rangle$ in E1 at $x = 0$; contour levels = (contour spacing, minimum, maximum) = (5×10^{-3}, -7.48×10^{-3}, 2.98×10^{-2}); (*b*) profile of $\langle -\lambda_2 \rangle$ along the line shown in (*a*).

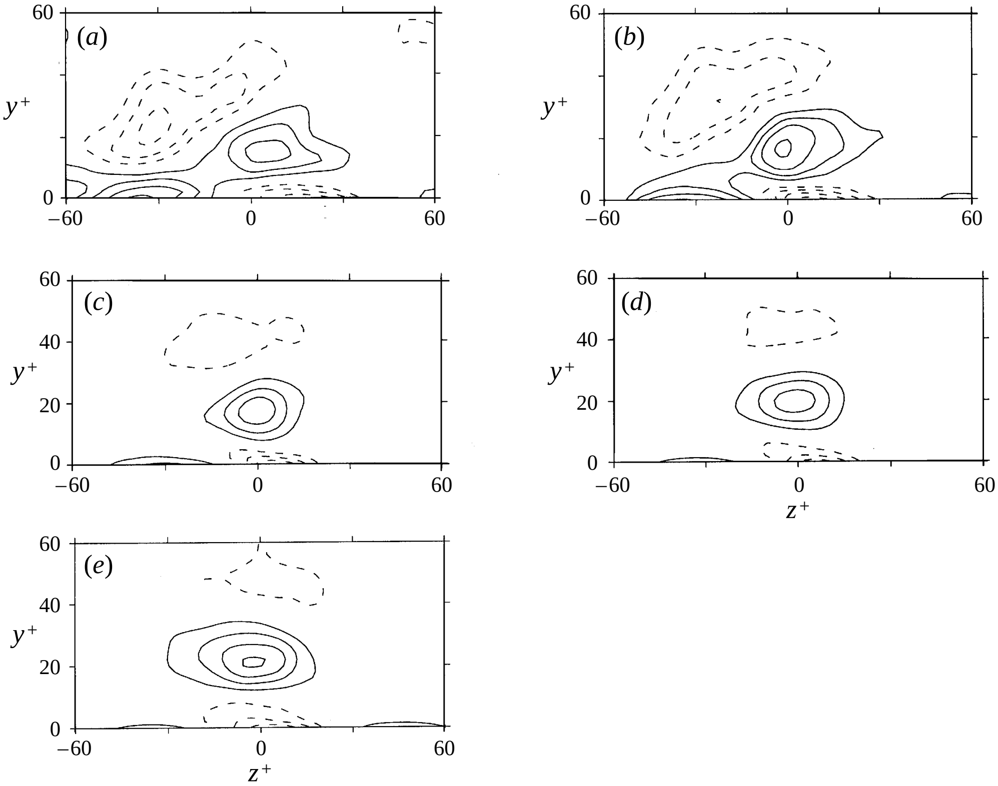

FIGURE 9. Contours of $\langle \omega_x \rangle$ showing the relative arrangement of SP and SN at various x locations in E2: (*a*) $x^+ = -60$, contour levels = (3×10^{-2}, -0.112, 0.128); (*b*) $x^+ = -30$, contour levels = (4×10^{-2}, -0.179, 0.167); (*c*) $x^+ = 0$, contour levels = (8×10^{-2}, -0.319, 0.292); (*d*) $x^+ = 30$, contour levels = (9×10^{-2}, -0.312, 0.32); (*e*) $x^+ = 60$, contour levels = (6×10^{-2}, -0.227, 0.247).

(§3). To see how SN is spatially related to SP, we define another ensemble average, E2, with the alignment point located near the upstream end of SP, using the same eduction procedure as for E1.

Contours of $\langle \omega_x \rangle$ obtained by E2 at various streamwise locations show that SN is located to the left and above the upstream end of SP (figure 9*a–e*). In figure 9(*a*), it might appear that this plane cuts through the legs of a possible hairpin structure. However, the downstream end of SN is not alongside SP in the spanwise direction, as shown in figure 9(*c–e*); instead, the inclined SP and SN structures overlap in x, as shown in figure 6. The contour strength of SN decreases in x while that of SP increases. Thus, figure 9(*a–e*) indicates not only the relative tilting of SP and SN in the (x, z)-plane, but also their relative shift in x. Note the near-wall vorticity layers of opposite signs induced by SP and SN underneath each. The CS geometry in figure 6 is apparently representative of instantaneous vortex realizations as well (Brooke & Hanratty 1993). The direction of tilting of SN is opposite to that of SP due to mutual induction between SP and SN; this is discussed in detail in the following section.

4.1. *Conceptual model of the dynamics of CS*

From the spatial relationship between SP and SN discussed above, we have developed a conceptual model to explain observed kinematic features, as shown schematically in figure 10(*a–d*) for the educed CS details (see also Jeong & Hussain 1992). This near-wall CS model consists of a train of quasi-streamwise structures with alternating signs of ω_x, which are inclined in the (x, y)-plane (figure 10*b*) and tilted in the (x, z)-plane (figure 10*a*). These SP and SN structures, located in the buffer region, overlap in x. In figure 10(*a*), we schematically show the spatial locations of internal shear layers E and H, of a kinked low-speed streak, and of Q2 and Q4 events with respect to structures SP and SN. An expanded view of an overlapping region between structures SP and SN is given in figure 10(*d*), where the locations of Q1 and Q3 events are also shown, along with the internal shear layers represented by typical points E and H in figure 10(*a*). In this model, the observed bursting process is the passage of several SP and SN past a fixed measurement location, in which the relative arrangement of the tilted structures creates a series of several ejection/sweep events; the multiple ejections found by Bogard & Tiederman (1986) during bursting are also consistent with the scenario depicted in figure 10(*a*).

The observed tilting of SP and SN can be explained in terms of their mutual induction, which, for instance, advects point A of an SN structure C in the negative z-direction and its point B in the positive z-direction (figure 10*a*). Thus, the effect of mutual induction is to *precess* SN in the clockwise direction and SP counterclockwise in the (x, z)-plane; the mutual induction between the overlapping CS in the section FG in figure 10(*a*) is implicit in figure 10(*c*). However, there is a countering effect due to the background shear $U(y)$ which acts to precess SN counterclockwise because the right-hand side of SN is at a higher y and hence moves downstream with a higher velocity than the left-hand side (i.e. the downstream end of SN advects in x faster than its upstream end), as shown schematically in figure 10(*e*). The end result of these counteracting precessions is a nearly constant tilting angle θ; thus, the CS does not precess, but is stretched along its own axis at the same θ.

In our conceptual model, internal shear layers containing positive and negative $\partial\langle u\rangle/\partial x$ are seen to result from the induction by SP and SN because of their tilting and overlap in the normal (x, y)-plane facilitated by their inclination. In figure 10(*a*), a VISA (Variable Interval Spatial Average – the spatial version of VITA) event with negative $\partial\langle u\rangle/\partial x$ occurs (at a typical point E) between structures C and D. The shear layer is created as structure C induces motion toward the wall (hence higher $\langle u\rangle$) upstream of E, while structure D induces velocity away from the wall (hence lower $\langle u\rangle$) downstream of E. The associated u-velocity fluctuations are positive and negative, upstream and downstream of E respectively, resulting in negative $\partial\langle u\rangle/\partial x$; this event is captured in ensemble average E2 and shown in figure 11(*a*) by an (x, y)-plane located away from the nose of SP in negative z. We find that VISA events with positive $\partial\langle u\rangle/\partial x$ occur at the midpoint of SP's streamwise extent (e.g. at point H in

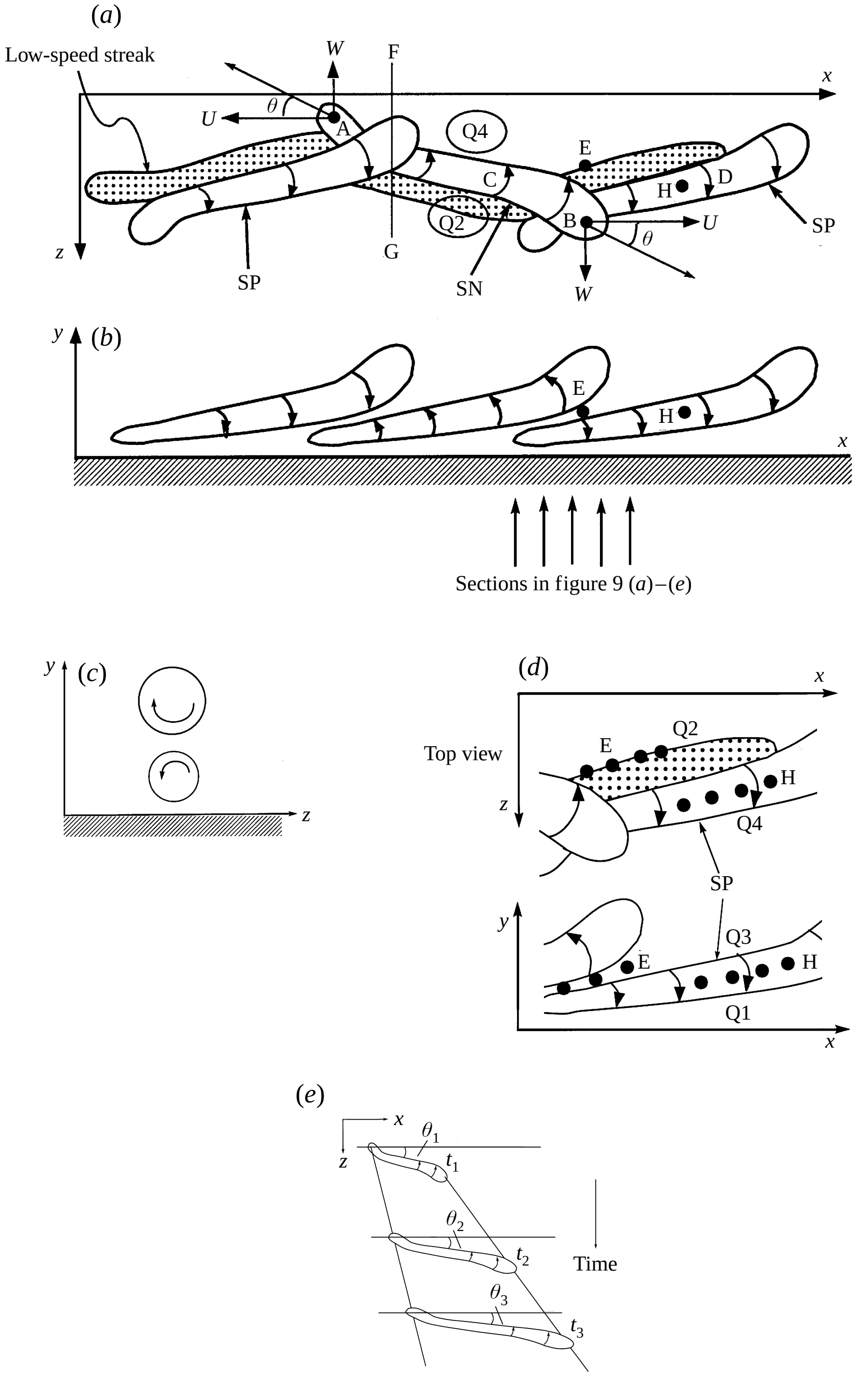

FIGURE 10. Conceptual model of an array of CS and their spatial relationship with experimentally observed events discussed in the text: (*a*) top view; (*b*) side view; (*c*) structures at cross-section FG in (*a*); (*d*) expanded views of structures C and D in (*a*,*b*), showing the relative locations of Q1, Q2, Q3, Q4, E and H. A schematic demonstrating the counteracting precession of SN in the (x, z)-plane due to background shear is shown in (*e*). The arrows in (*b*) denote the sections of figure 9(*a*–*e*).

figure 10*a*), since ejection (negative $\langle u\rangle$) occurs upstream of SP and sweep (positive $\langle u\rangle$) occurs downstream of SP, as is also the case for SN; i.e. positive $\partial\langle u\rangle/\partial x$ occurs at the centres of SP and SN. This event is well captured at the alignment point (i.e. H in figure 10*a*) of ensemble average E1, as shown in figure 11(*b*). The asymmetry of u-fluctuations about $z = 0$ in the internal shear layer (VISA events at E and H) is clearly seen in contours of $\langle u - U(y)\rangle$ from ensemble average E2 (figure 11*c*); here $U(y)$ is the space- and time-averaged streamwise velocity. Some regions of E and H are qualitatively shown in figure 11(*a–c*). The figure shows a strong resemblance to the results of Johansson *et al.* (1991), who used a conditional VISA sampling technique to study internal shear layers such as E and H. Note that these events were not used *a priori* in the ensemble averaging; thus, their presence in our ensemble average triggered by λ_2-based CS detection confirms the validity of the proposed conceptual model.

The positive $\partial\langle u\rangle/\partial x$ (which implies negative $\partial\langle u\rangle/\partial t$ from Taylor's hypothesis) regions in figure 11(*b*) are weaker than the negative $\partial\langle u\rangle/\partial x$ (i.e. positive $\partial\langle u\rangle/\partial t$) events in figure 11(*a*) (cf. contour levels and contour slope with respect to x), an observation which can be explained as follows. Once a VISA event with positive $\partial\langle u\rangle/\partial x$ (i.e. negative $\partial\langle u\rangle/\partial t$ – a negative VITA event) occurs, the magnitude of positive $\partial\langle u\rangle/\partial x$ weakens due to the underlying velocity field. Namely, a low-speed fluid particle upstream moves slower than a high-speed fluid particle downstream, causing the distance between them to increase in time, so that $\partial\langle u\rangle/\partial x$ decreases. For negative $\partial\langle u\rangle/\partial x$ regions, the high-speed fluid upstream moves faster than the low-speed fluid downstream, thereby creating a steeper gradient. This is consistent with the negative skewness factor of $\partial u/\partial x$ observed in most turbulent flows. The stronger negative $\partial\langle u\rangle/\partial x$ in our educed fields is also consistent with the experimental result that the frequency of occurrence of negative VISA events (positive VITA events) is higher than that of positive VISA events (negative VITA events) for the same $|\partial\langle u\rangle/\partial x|$ threshold.

4.2. *Effect of phase difference between velocity components*

In this section, we discuss the relative spatial locations of large u- and v-fluctuations, hereinafter called their *phase difference* (for the lack of a better descriptor), with regard to Reynolds stress generation.

The velocity fields $\langle u - U\rangle$ and $\langle v\rangle$ in the $x = 0$ plane through SP have similar patterns (figure 12*a,b*). Since variations in $\langle u - U\rangle$ result from the advection of fluid across the shear region induced by CS, negative u tends to accompany positive v and vice versa. Thus, in figure 12, we can assign a Q2 event to the left of the CS and a Q4 event on its right. Nevertheless, a phase difference between the locations of peak u- and v-fluctuations is evident in figure 12, which has important implications for the Reynolds stress distribution, as discussed below.

To explain this phase difference, we consider an inviscid streamwise vortex embedded in a homogeneous shear flow $U(y)$ with a shear rate $\mathrm{d}U/\mathrm{d}y = S$. This simplification enables an analytical solution, because $\mathrm{D}u/\mathrm{D}t = 0$ and the particle pathline has a simple analytical form. The evolutions of the u-, v- and w-fluctuations can be shown to be

$$u(r,\theta,t) = Sr\left[\sin(f(r)t/r + \theta) - \sin\theta\right] = 2Sr\cos\left(\theta + \frac{f(r)t}{2r}\right)\sin\left(\frac{f(r)t}{2r}\right),$$
$$v(r,\theta,t) = f(r)\cos\theta, \quad \text{and} \quad w(r,\theta,t) = f(r)\sin\theta.$$

Here r is the distance from the centre of the vortex, θ is the angle with respect

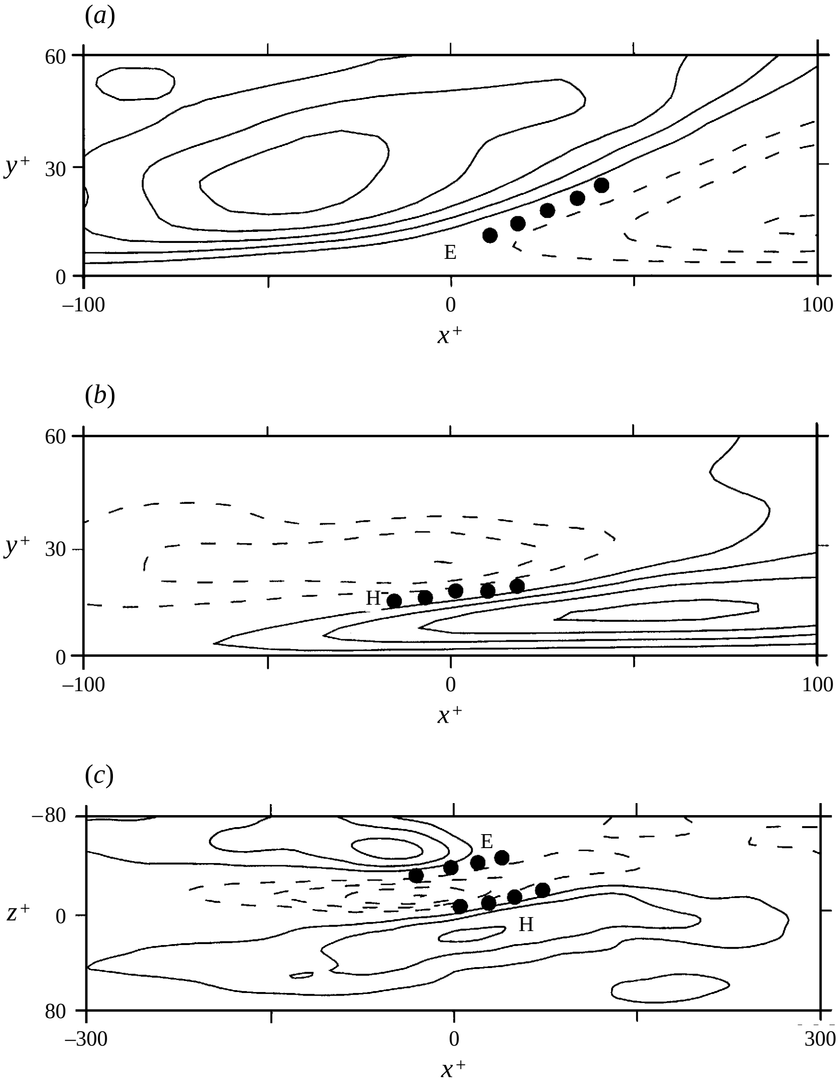

FIGURE 11. (*a*) $\langle u-U\rangle$ in E2 at $z^+=-40$, contour levels = (0.4, −1.25, 2.14); (*b*) $\langle u-U\rangle$ in E1 at $z^+=0$, contour levels = (0.3, −0.947, 1.68). (*c*) $\langle u-U\rangle$ in E2 at $y^+=15$, contour levels = (0.4, −1.21, 1.71). Locations of internal shear layers E and H in figure 10(*a*,*b*) are also qualitatively indicated.

to the x-axis, and $f(r)$ is the initial azimuthal velocity profile. When t is small, $u \approx Sf(r)t\cos\theta$, so that the u and v velocities are in phase; however, as t increases, a phase difference emerges. By comparing u and v above, the phase difference $\Delta\theta$ between u and v velocities (computed from the locations of maximum u and v) is seen to be $\Delta\theta = f(r)t/(2r)$, indicating linear growth in time (at fixed r). For a developed quasi-streamwise vortex, this phase difference is expected to be non-negligible; hence the non-negligible Q1 and Q3 events. This effect also causes the negative peak of $\langle u-U\rangle$ to occur at a larger y^+ than the positive peak of $\langle u-U\rangle$, irrespective of the sign of ω_x (figure 12*a*). Thus, Q4 is observed more frequently than Q2 near the wall and vice versa away from the wall.

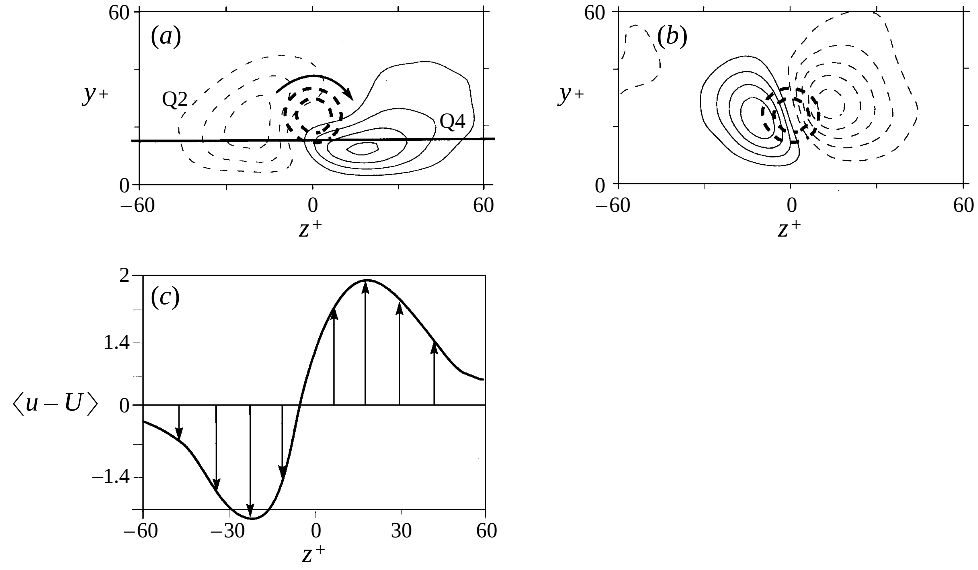

FIGURE 12. Coherent velocities at $x = 0$ in E1: (*a*) $\langle u - U\rangle$, contour levels = (0.7, −2.60, 2.96); (*b*) $\langle v\rangle$, contour levels = (0.2, −1.10, 0.978); (*c*) profile of $\langle u - U\rangle$ along the line in (*a*). Thick contours denote the educed CS centre for ensemble average E1.

Coherent normal velocity $\langle v\rangle$ contours at $x = 0$ in figure 12(*b*) show positive and negative values on the left- and right-hand sides of SP respectively, as expected. However, $\partial\langle v\rangle/\partial y$ is negative at the centre of SP; in other words, the zero crossing of $\langle v\rangle$, which bounds regions of Q1 and Q3 events, is rotated through a counterclockwise angle. This feature is seen to be a consequence of the CS tilting in the following way. Since the tilting of SP and SN creates negative $\langle u - U\rangle$ upstream and positive downstream of both SP and SN, $\partial\langle u\rangle/\partial x$ is positive at the structure centre (e.g. point H in figure 10*a*). In addition, examination of the educed flow field reveals that $\partial\langle w\rangle/\partial z$ near the structure centre is small (since $\langle w\rangle$ is symmetric in z at H) compared to $\partial\langle u\rangle/\partial x$. Thus, it follows from the continuity equation that $\partial\langle v\rangle/\partial y$ is negative at the structure centre (figure 12*b*).

The coherent Reynolds stress $-\langle u - U\rangle\langle v\rangle$ is positive nearly everywhere (figure 13*a*), as would be expected from Prandtl's mixing length theory. Nevertheless, a small region of negative coherent Reynolds stress is present due to the (spatial) phase difference between $\langle u - U\rangle$ and $\langle v\rangle$. For example, $\langle v\rangle$ is negative above the structure centre, where $\langle u - U\rangle$ is also negative; the latter follows from the fact that fluid above the structure has been advected from near the wall and thus contains smaller x-momentum. Thus, Q3 events occur above the structure centre, and, by the same token, Q1 events occur below the structure centre. The observation that Q1 and Q3 events are much less probable than Q2 and Q4 events (Willmarth & Lu 1972; Kim *et al.* 1987) is consistent with the relatively small area of negative coherent Reynolds stress observed in our educed fields.

It is interesting to note that the other components of coherent Reynolds stress have a different symmetry. Contours of $-\langle v\rangle\langle w\rangle$ show a cloverleaf pattern with alternating sign (figure 13*b*), so that the net (i.e. spatial-averaged) Reynolds stress, $-\langle v\rangle\langle w\rangle$, nearly vanishes. In contrast, $-\langle u - U\rangle\langle w\rangle$ is predominantly positive for SP (figure 13*c*) due to a phase difference between $\langle u - U\rangle$ and $\langle w\rangle$. However, this positive value is

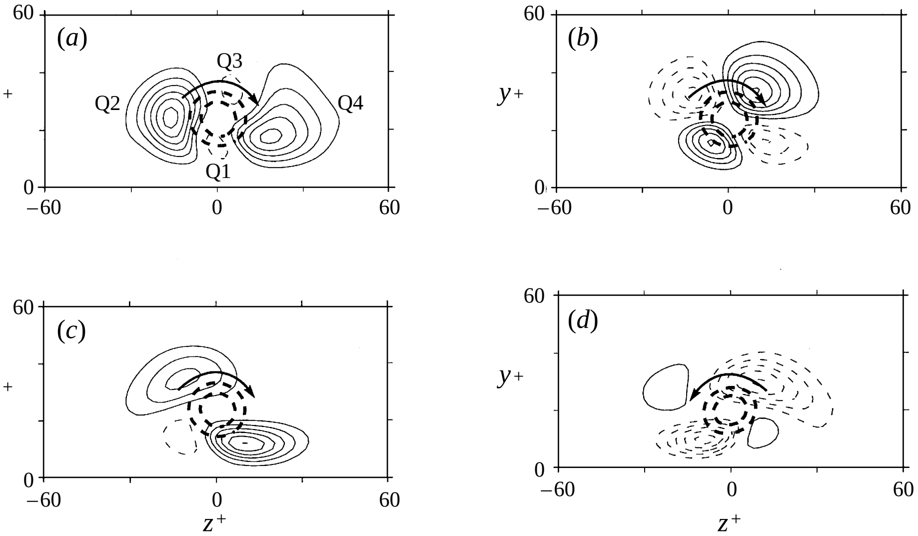

FIGURE 13. Coherent Reynolds stresses at $x = 0$ in E1: (*a*) $-\langle u - U\rangle\langle v\rangle$ for SP, contour levels = (0.3, −0.534, 1.94); (*b*) $-\langle v\rangle\langle w\rangle$ for SP, contour levels = (0.2, −0.868, 1.22); (*c*) $-\langle u - U\rangle\langle w\rangle$ for SP, contour levels = (0.7, −1.34, 4.23); (*d*) $-\langle u - U\rangle\langle w\rangle$ for SN. Relative locations of Q1, Q2, Q3 and Q4 events with respect to the CS center are shown in (*a*).

compensated by the negative $-\langle u - U\rangle\langle w\rangle$ produced by SN (figure 13*d*). Since, as expected, SP and SN are distributed in the buffer region with equal probability and their contributions are equal and opposite, the time-averaged Reynolds stress $-\overline{uw}$ vanishes.

Thus, analysis of induced velocities can explain the regions around a CS which cause Q1, Q2, Q3 and Q4 events. In addition, instantaneous coherent Reynolds stress patterns with respect to the CS centre are documented. Although they have clear spatial distributions, only $-\langle u - U\rangle\langle v\rangle$ produces a non-zero spatial average. The $-\langle u - U\rangle\langle w\rangle$ and $-\langle v\rangle\langle w\rangle$ distributions have spatial variations but have small spatial averages when both SP and SN are accounted for.

4.3. *Vortex lines near CS*

To investigate the vortex line geometry in our ensemble-averaged field, vortex lines are traced upstream and downstream of SP (figure 14*a*). We observe that hairpin vortex lines occur upstream of the structure and that inverted hairpin vortex lines occur near its downstream end, even though the structure is neither hairpin nor inverted hairpin shaped.

The inclination angle $\tan^{-1}(\langle\omega_y\rangle/\langle\omega_x\rangle)$ of the vorticity vector at the centre of SP, i.e. the location of peak λ_2, is about 17°. This is significantly higher than the inclination angle of SP indicated by isosurfaces of $\langle\lambda_2\rangle$, which is 9°. The difference in the angle of the vorticity vector and that of the structure axis is a simple consequence of the intrinsic difference between vorticity surfaces and vortex surfaces (Melander & Hussain 1994) and can be explained by the following considerations. Consider a vortical structure aligned with x in the presence of a background shear $U(y)$ (with $\omega_z < 0$). The evolution of the normal (to the vortex axis) component of the vorticity vector is given by

$$\frac{\mathrm{D}\omega_n}{\mathrm{D}t} = \omega_z\frac{\partial u_n}{\partial z} + \omega_n\frac{\partial u_n}{\partial n} + \omega_s\frac{\partial u_n}{\partial s}. \tag{4.1}$$

For simplicity, suppose that $\omega_n = 0$ initially and note that $\partial u_n/\partial s$ is negligible for a streamwise-aligned elongated vortex (identically zero for an infinite vortex tube). For a vortex with positive ω_s (i.e. SP), its induced velocity u_n is negative (positive) at larger (smaller) z than the plane of figure 14(*b*); thus, $\partial u_n/\partial z$ is negative across the CS. Since ω_z is negative everywhere due to the background shear, positive ω_n is generated according to (4.1) even if ω_n is not present initially. Therefore, the vorticity vectors inside a vortical structure in the presence of mean shear generally deviate from the axis of the vortical structure itself. This effect is clearly demonstrated in the ensemble-averaged flow in figure 14(*c*) for SP by vortex lines (lines everywhere tangent to the vorticity vector) passing through several locations along the CS axis. These vortex lines immediately deviate from the CS axis, exit the CS core at an angle to the $\lambda_2 = 0$ surface, and align with the nearly orthogonal vortex lines of the background shear outside the core. This behaviour of vortex lines has also been observed in homogeneous shear flow turbulence (Kida & Tanaka 1994). Similarly, this effect is responsible for the vortex line shape in a (y, z)-projection shown in figure 14(*d*).

In an alternative, more physical approach, this difference between the vortex core angle and vorticity vector angle can be interpreted in terms of the inviscid turning of vortex lines. For instance, consider vortex lines L_a, L_b and L_c in figure 14(*e*,*f*), which are initially straight in a (y, z)-projection. Due to the induced vortical motion, these lines deform as shown schematically in figure 14(*g*,*h*), producing a vortex line geometry which is consistent with the ensemble-averaged field (see the similarities of the vortex lines in figure 14*g*,*h* with those in figure 14*c*,*d*). Note that no change is observed in the (x, z)-projection since ω_x cannot be created nor destroyed in this idealized x-independent, inviscid flow.

In summary, vortex lines starting even on the axis of the vortex immediately deviate from this axis and eventually cross the vortex core boundary, i.e. the $\lambda_2 = 0$ surface (figure 14*c*,*d*). Therefore, it is not possible to accurately characterize a streamwise vortical structure subjected to a strong background shear by a vortex line tracing technique.

4.4. *Effect of the structure on the background vorticity field*

Swearingen & Blackwelder (1987) pointed out that spanwise inflectional profiles of $u(z)$ are common and suggested that inviscid instability of $u(z)$ is responsible for the genesis of near-wall turbulence; Antonia & Bisset (1990) experimentally found that such a $u(z)$ profile does in fact exist during the bursting process. To address this issue, we relate the locations of $\partial\langle u\rangle/\partial z$ peaks (spanwise inflection points of u) and $\langle\omega_z\rangle$ to SP.

Contours of $\langle\omega_z\rangle$ at $x = 0$ (figure 15*a*) show high-shear (M) and low-shear (N) regions resulting from cross-stream advection by SP. The spanwise vorticity fluctuation $\langle\omega_z - \Omega_z\rangle$ changes its sign in z near the wall (figure 15*b*); this is consistent with predominantly negative near-wall values of the correlation $R_{\omega_z\omega_z}(y, \Delta z; y_{ref} = 20)$ of ω_z fluctuations and the weaker positive $R_{\omega_z\omega_z}$ with $-z$ separation (figure 15*c*).

We find that the maximum $\partial\langle u\rangle/\partial z$ occurs at the bottom left of the structure centre (figure 15*d*), and that $\langle\omega_y\rangle \approx \partial\langle u\rangle/\partial z$, as can be seen by comparing figure 15(*d*,*e*) (i.e. $\partial\langle w\rangle/\partial x$ is negligible). As mentioned in §4.3, ω_y is created from the reorientation of ω_z by the induced motion of the structure (see figure 14*f*,*h*), which results in a positive peak of ω_y at the bottom left of the structure, producing the inflection of $u(z)$ shown in figure 12(*c*); this effect will be demonstrated in more detail below using an inviscid model. In figure 15(*f*), a conditional two-point correlation $R_{\omega_y\omega_y}(y, \Delta z; y_{ref} = 20)$,

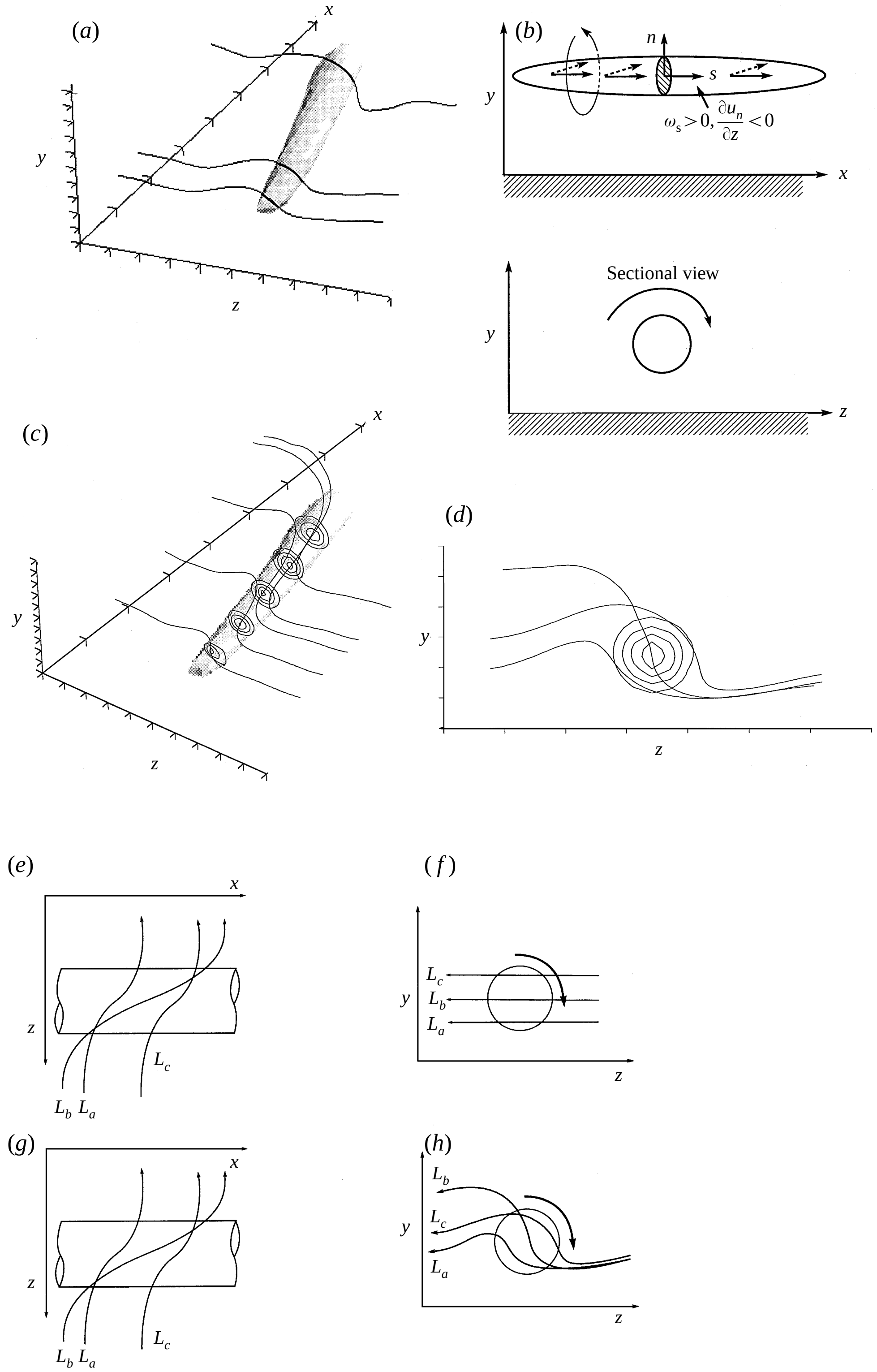

FIGURE 14. For caption see facing page.

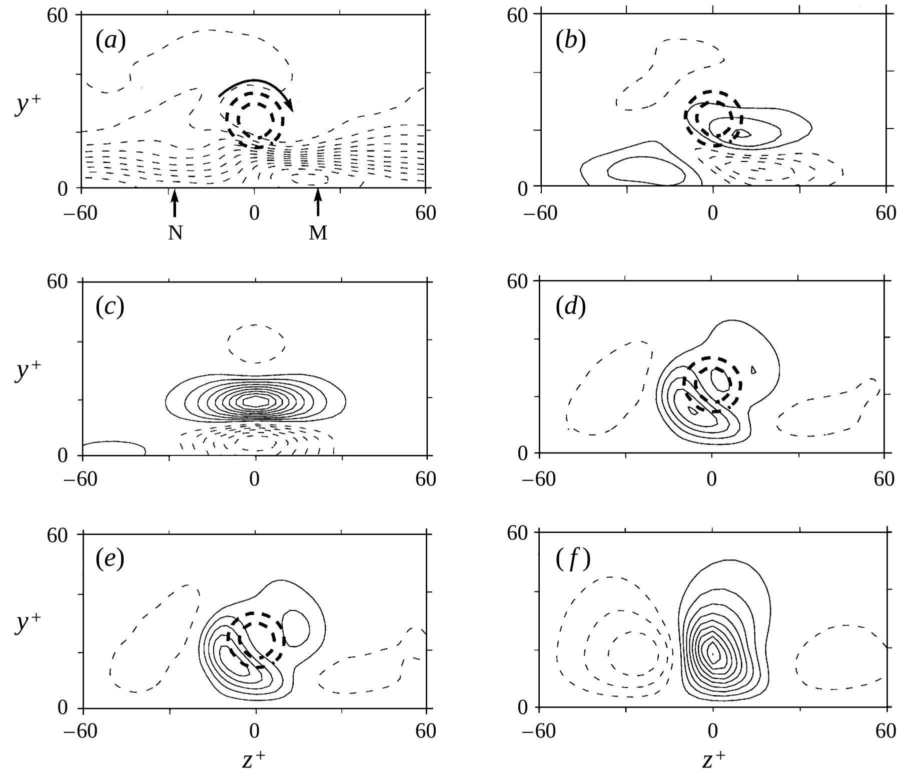

FIGURE 15. (*a*) $\langle \omega_z \rangle$ at $x = 0$ in E1, contour levels = (0.1, −1.24, 9.85×10^{-3}). (*b*) $\langle \omega_z \rangle - \mathrm{d}U/\mathrm{d}y$. (*c*) $R_{\omega_z\omega_z}(y, \Delta z; y_{ref} = 20)$. (*d*) $\partial \langle u \rangle / \partial z$ at $x = 0$ in E1. (*e*) $\langle \omega_y \rangle$ at $x = 0$ in E1, contour levels = (0.05, -9.79×10^{-2}, 0.285). (*f*) Conditional correlation $R_{\omega_y\omega_y}(y, \Delta z; y_{ref} = 20)$.

defined as

$$R_{\omega_y\omega_y}(y, \Delta z; y_{ref} = 20) = \int \omega_y(x, z; y_{ref})\omega_y(x, z + i\Delta z; y_{ref})\mathrm{d}x\mathrm{d}z,$$

where

$$i = \begin{cases} 1 & \text{for } \omega_x(x, y_{ref}, z) \geqslant 0; \\ -1 & \text{for } \omega_x(x, y_{ref}, z) < 0, \end{cases}$$

shows that negative peaks exist on both sides of the structure; this is consistent with the ensemble average $\langle \omega_y \rangle$, providing additional evidence that the educed flow captures instantaneous flow features related to the presence of streamwise vortices.

To obtain a clearer picture of the evolutions of u, ω_y, and ω_z produced by a quasi-streamwise vortex subjected to shear, we now consider the top half of an inviscid streamwise Batchelor dipole embedded in a shear flow, with the same mean streamwise velocity profile $U(y)$ as in the turbulent channel flow (see schematic in

---

FIGURE 14. (*a*) Vortex lines traced outside CS from $(x^+, y^+, z^+) = (-100, 20, 170)$, $(-70, 24, 170)$ and $(100, 45, 170)$. (*b*) Notation for the explanation of different inclination angles of a vortex core and vortex lines; solid arrows denote initial vorticity vectors; dotted arrows denote later-stage vorticity vectors. (*c*) Vortex lines traced through the CS axis. (*d*) Front view of vortex lines passing through the vortex centre and its top and bottom. (*e–h*) Schematic evolution of vortex lines (L_a, L_b, L_c) for a streamwise vortex in a pure shear flow $U(y)$: (*e–f*) initial instant; (*g–h*) later stage.

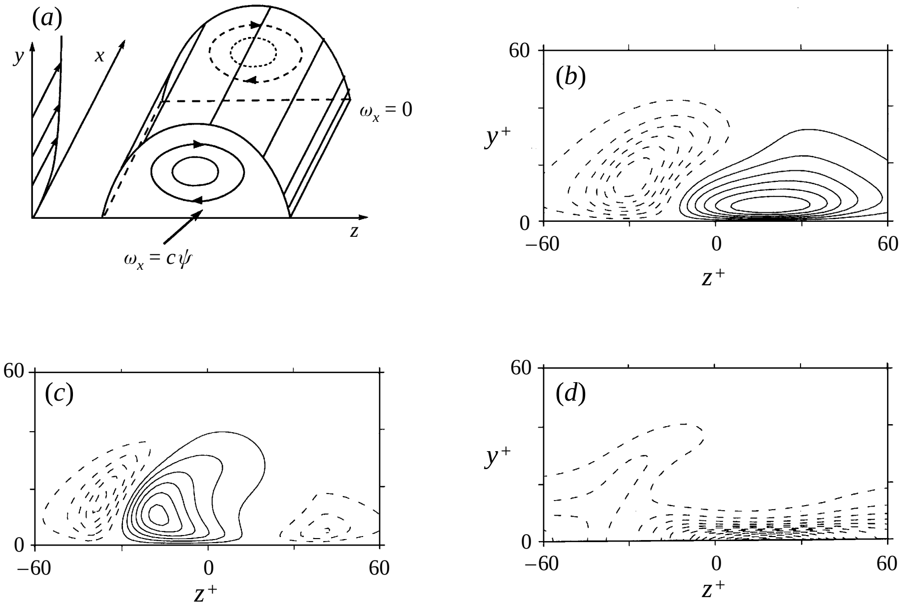

FIGURE 16. Evolution of an inviscid streamwise vortex in a non-uniform shear $U(y)$ at $t = 20$. (*a*) Schematic of Batchelor's vortex. (*b*) $(u - U)$, contour levels = (0.8, −5.57, 5.58). (*c*) ω_y, contour levels = (0.06, −0.32, 0.39). (*d*) ω_z, contour levels = (0.2, -3.24×10^{-2}, 3.30).

figure 16*a*). The Batchelor dipole exhibits steady v- and w-velocities in a reference frame moving with the dipole propagation velocity.

The streamfunction for the dipole is given by $\psi = -cJ_1(kr)\sin\theta$ (Batchelor 1967, p. 535), where $\partial\psi/\partial z = -v$, $\partial\psi/\partial y = w$, with $r = (y^2 + z^2)^{1/2}$ and $\theta = \tan^{-1}(y/z)$. We prescribe the vortex centre (defined as the point of minimum ψ) to be located at $y^+ = 20$ in the non-uniform shear profile $U(y)$. The parameters c and k are set as 7 and 0.5 wall units respectively, in order to centre the Batchelor dipole at $y^+ = 20$ and to produce the same circulation as the ensemble-averaged structure. With these parameters, the spanwise velocity of the dipole is $0.28u_*$. The assumption of an inviscid flow is justified for short times since the viscous time scale is about 200 wall units. For this flow, the inviscid momentum equations become

$$\frac{\partial u}{\partial t} + v\frac{\partial u}{\partial y} + w\frac{\partial u}{\partial z} = 0, \tag{4.2}$$

$$\frac{\partial v}{\partial t} + v\frac{\partial v}{\partial y} + w\frac{\partial v}{\partial z} = -\frac{\partial p}{\partial y}, \tag{4.3}$$

$$\frac{\partial w}{\partial t} + v\frac{\partial w}{\partial y} + w\frac{\partial w}{\partial z} = -\frac{\partial p}{\partial z}. \tag{4.4}$$

Equations (4.3) and (4.4) are decoupled from (4.2), so that the flow in the (y, z)-plane can be easily solved using the initial Batchelor dipole velocity field. From (4.2), the u-velocity of a particle at time t is the same as its initial velocity, so that the u-velocity for each point in the (y, z)-plane at time t is easily computed by integrating the particle path backwards in time. Interestingly, the distributions of $(u - U)$, ω_y and ω_z at $t = 20$ in figure 16(*b*–*d*) resemble well those from the ensemble average educed from the turbulent case (cf. figures 12*a*, 15*e* and 15*a* respectively), implying that the basic mechanism responsible for their evolution is inviscid cross-stream vortical advection.

Note that a non-zero spanwise slip velocity w at the wall in the inviscid model does not produce significant differences from the ensemble-averaged data for u, ω_y and ω_z; the slip velocity at the wall does not create u-fluctuations during advection since no u-variation along the wall is present.

To summarize, we find that viscosity and CS three-dimensionality are not essential features influencing the background shear, ω_y- and ω_z-distributions. Instead, these distributions are determined simply by inviscid, basically two-dimensional advection induced by SP and SN, and projected on the (y, z)-plane. Nevertheless, three-dimensional effects (i.e. x-dependence) are crucial to the sustaining of CS, as discussed in §4.7.

4.5. *Turbulence production and intensity*

To gain insight into near-wall incoherent (small-scale) turbulence production by CS, we consider separately the turbulence production P_t (i.e. the production of incoherent motion by coherent motion) and the production P_c of coherent motion due to the mean flow, derived by Hussain (1983*a*) as

$$P_t = -\sum_{i,j} \langle u_{ri} u_{rj} \rangle \langle S_{ij} \rangle, \quad P_c = -\langle u - U \rangle \langle v \rangle \frac{\mathrm{d}U}{\mathrm{d}y}.$$

Since P_t, shown for the plane $x = 0$ of SP in figure 17(*a*), captures the creation of incoherent motion (with smaller scales), peaks of P_t indicate probable locations of secondary, irregularly appearing vortices. The peaks of incoherent turbulent kinetic energy $\langle q_r^2 \rangle = \langle u_r^2 + v_r^2 + w_r^2 \rangle$ (figure 17*b*) and those of P_t coincide, implying that incoherent turbulence does not accumulate in the structure centre (unlike free shear flows; see Hussain 1983*b*). Instead, incoherent turbulence, once produced, decays as it is convected by the coherent motion. This is consistent with the scale dependence of the propagation velocity of turbulence fluctuations near the wall found by Kim & Hussain (1993). From two-point correlations of vorticity and velocity fluctuations with time delay, they inferred that near-wall turbulence with large k_z (small spanwise scale) moves faster in z than that with small k_z (large spanwise scale). For incoherent turbulence to accumulate at the structure centre, the propagation velocity of the small-scale turbulence would have to be comparable with that of the large-scale structures, since both the large and small scales would be moving together in this case. Thus, the fact that $\langle q_r^2 \rangle$ has a local maximum outside the CS and closer to the wall is consistent with this scale dependence of the propagation velocity. The CS moves slower in the spanwise direction than the small scales advected by it along the wall, because of the CS's larger distance from the wall (and thus its image structure).

The location of peak P_t at $y^+ \approx 30$ does not match that of the time-averaged turbulence production (i.e. production of fluctation kinetic energy, with Reynolds averaging), which occurs at $y^+ \approx 13$ (Klebanoff 1954; Kline *et al.* 1967; Kim *et al.* 1987); this suggests that P_t is not a dominant contribution. On the other hand, peaks of P_c in figure 17(*c*) occur on both sides of SP at $y^+ \approx 13$, implying that buffer-layer CS are responsible for most of the mean turbulence production. Note that for triple decomposition of the velocity field into mean, coherent, and incoherent components, the mean turbulence production is equivalent to the sum of time-averaged coherent and incoherent turbulence productions (Hussain 1983*a*). The negative P_c appearing locally at the bottom of SP (figure 17*c*) is due to negative coherent Reynolds stress Q1, which in turn results from the phase difference between $\langle u \rangle$ and $\langle v \rangle$, as discussed in §4.2.

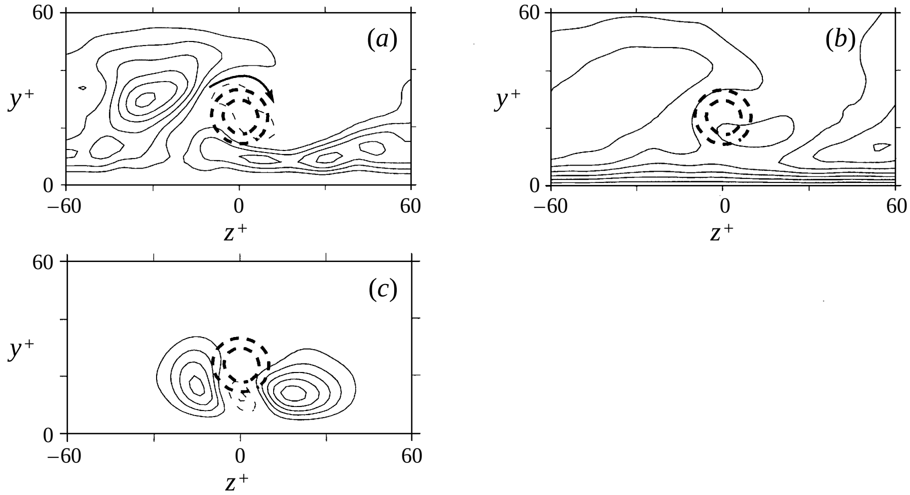

FIGURE 17. Turbulence productions and incoherent turbulence intensity at $x = 0$ in E1. (*a*) Production P_t of incoherent motion by coherent motion, contour levels = (0.05, -4.21×10^{-2}, 0.313). (*b*) Incoherent turbulence intensity $\langle u_r^2 + v_r^2 + w_r^2 \rangle$ contour levels = (0.4, 2.89×10^{-5}, 2.82). (*c*) Production P_c of coherent motion due to the mean flow, contour levels = (0.1, −0.222, 0.557).

4.6. *The effect of near-wall CS on wall pressure*

The wall pressure distribution reflects the presence of streamwise vortices in the buffer region and can conceivably be used to sense their locations for developing adaptive control techniques. For SP, the coherent pressure fluctuation is negative below the CS and positive on both sides of the structure (figure 18*a*), where fluid is pumped either toward or away from the wall. Note that the symmetry (dotted) line of negative $\langle p \rangle$ contours on the wall deviates from the 4° tilt of SP shown in figure 18(*a*). However, since the wall pressure is the combined influence of overlapping SP and SN structures (see figure 10*a*,*b*), the deviations at the front and back ends of $\langle p \rangle$ contours are to be expected. The cross-correlation $R_{pp}(\Delta x, \Delta z\,; y_{ref} = 0)$ in figure 18(*b*) shows negative values for sufficient x-separation, which is consistent with the variation of $\langle p \rangle$ in x. However, in contrast to $\langle p \rangle$, R_{pp} does not show negative values with separation in z (figure 18*b*). This difference can be explained in terms of the long-range influence of outer-scale structure on the wall pressure. Consider an outer-scale structure above inner-scale buffer region vortices as shown in figure 18(*c*). In this case, the wall pressure contribution from the near-wall structures is negative immediately below the CS and positive farther away. The outer-scale structure contributes negative pressure with a larger spanwise scale; thus, the resultant wall-pressure is negative for a large spanwise extent (with some fluctuations) and the two-point correlation (figure 18*b*) is not negative in the spanwise direction.

For the ensemble-averaged pressure $\langle p \rangle$, uncorrelated outer-scale pressure contributions from outer structures are cancelled by the ensemble averaging of near-wall vortical events, so that only the inner-scale pressure remains. To confirm this, we removed the large-scale component of the wall pressure by removing the three smallest spanwise wavenumbers in Fourier space. The correlation of filtered wall pressure clearly shows negative values with z-separation (figure 18*d*), which is consistent with our ensemble-averaged wall pressure. This suggests that the wall pressure signal is strongly affected not only by near-wall structures, but also by outer structures; thus,

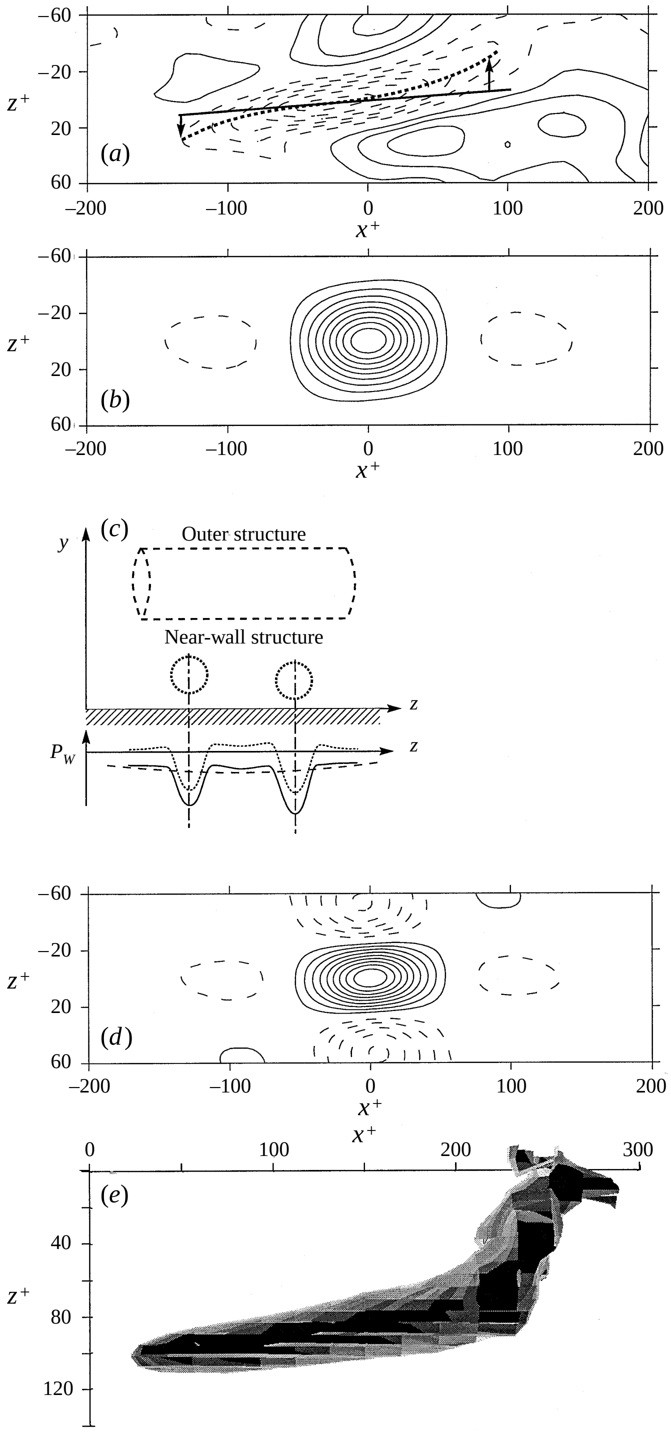

FIGURE 18. CS pressure field. (*a*) $\langle p\rangle$ at the wall, contour levels = (0.2, −1.28, 0.752); the dotted line denotes the locus of the local minima while the solid line represents the SP tilt angle of 4°. (*b*) $R_{pp}(\Delta x, \Delta z; y_{ref} = 0)$. (*c*) A schematic distinguishing the scale of pressure footprints from outer-region and buffer-layer structures. (*d*) $R_{pp}(\Delta x, \Delta z; y_{ref} = 0)$ of pressure after removing the largest 3 modes in the z-direction. (*e*) Isosurface of $\langle p\rangle = -0.3$ for SP.

caution should be exercised in ascertaining the locations of near-wall vortices from unconditioned wall pressure data alone. Away from the wall, a low-pressure region in $\langle p\rangle$ coincides with the spatial extent of the structure, as shown in figure 18(*e*). In addition, the low-pressure region near the downstream end of the CS shows a 'hook'-type geometry, similar to that suggested by Kline & Robinson (1989).

4.7. *Effect of CS on intercomponent energy transfer*

Using our educed flow field data, we now consider an energy transfer scenario responsible for CS formation and sustenance against dissipation. While vortex dynamics has provided significant insight into the dynamics of turbulent boundary layers in this and other studies, such an approach has not provided adequate information about energy transfer. For this purpose, we consider the turbulent kinetic energy equation to link the vortex dynamics discussed throughout this paper to the energy transfer mechanisms intrinsic to near-wall CS.

The mean streamwise component of pressure-strain $\overline{p\partial u/\partial x}$, responsible for the transfer of $\overline{u^2}$ kinetic energy to $\overline{v^2}$ and $\overline{w^2}$ components, is usually negative in turbulent shear flows (Tennekes & Lumley 1972). In near-wall turbulence, the tilting of SP and SN in the (x, z)-plane produces negative $\overline{p\partial u/\partial x}$ in the following manner. The tilting of SP and SN is responsible for positive $\partial\langle u\rangle/\partial x$ within the structure, as shown in §4.1. Since $\langle p\rangle$ is negative within the structure, $\langle p\rangle\partial\langle u\rangle/\partial x$ is also negative (figure 19*a*). Note that if SP were tilted in the opposite direction, then positive $\langle p\rangle\partial\langle u\rangle/\partial x$ would result.

Negative $\langle p\rangle\partial\langle u\rangle/\partial x$ also occurs in internal shear layers (e.g. point E in figure 10), as can be seen from ensemble average E2. Within the internal shear layer (denoted E$'$ in figure 19*b* corresponding to E in figure 10*a*), $\partial\langle u\rangle/\partial x$ is negative, and $\langle p\rangle$ is positive since the flow is locally decelerating, so that $\langle p\rangle\partial\langle u\rangle/\partial x$ is negative (figure 19*b*). Thus, redistribution of turbulent kinetic energy is active not only within the structure core but also near internal shear layers. The other energy transfer terms, $\langle p\rangle\partial\langle v\rangle/\partial y$ and $\langle p\rangle\partial\langle w\rangle/\partial z$ (figure 19*c*,*d*), show an interchange of v^2 and w^2 energies within the structure due to the CS's vortical motion.

The transfer of energy from the mean flow to each velocity fluctuation is schematically shown in figure 19(*e*). To illustrate, first consider fully developed streamwise vortices in the ensemble-averaged picture developed in this study. These CS transfer energy from the mean flow to u^2 by normal advection across the mean velocity gradient (see §4.4), during streak formation. The turbulent kinetic energy in u^2 is larger than that in v^2 and w^2, as seen in the ensemble-averaged velocity fluctuations (figure 12); this is also consistent with mean turbulent kinetic energy statistics. Simultaneously, the large energy in u^2 in the internal shear layer (E in figure 10; E$'$ in figure 19*b*) is transferred to v^2 and w^2 (mostly to w^2) through pressure–strain effects. Along with the production of streamwise vorticity by the mean flow (due to CS three-dimensionality), this feeds energy back into the streamwise vortices, to complete the process. Due to its qualitative nature, this intercomponent energy exchange scenario needs to be further explored via the underlying evolutionary vortex dynamics, which are beyond the scope of this paper and the subject of a separate investigation (Schoppa 1997).

5. Concluding remarks

Our newly defined vortex definition, based on the second largest eigenvalue of $S_{ik}S_{kj} + \Omega_{ik}\Omega_{kj}$ (developed to detect vortical structures in DNS data) has been successfully implemented as a conditional sampling scheme to educe near-wall CS. It

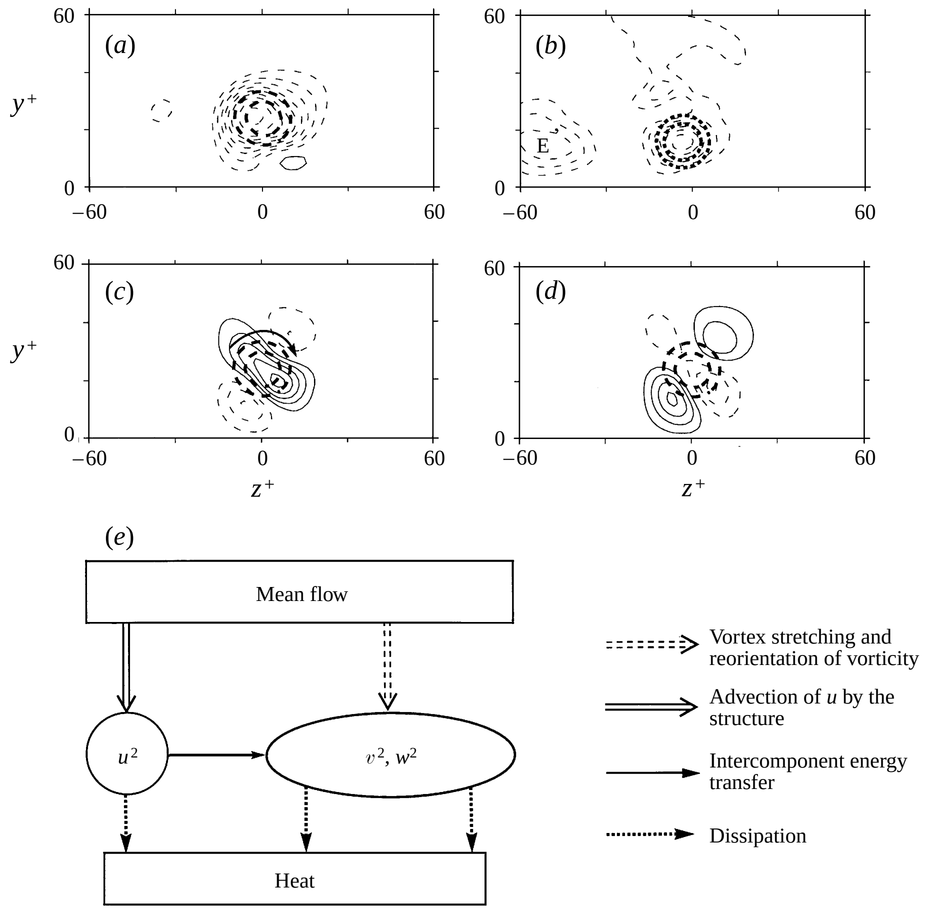

FIGURE 19. Coherent intercomponent energy transfer terms: (*a*) $\langle p\rangle\partial\langle u\rangle/\partial x$ at $x = 0$ in E1, contour levels = $(1 \times 10^{-2}, -9.51 \times 10^{-2}, 1.45 \times 10^{-2})$; (*b*) $\langle p\rangle\partial\langle u\rangle/\partial x$ at $x = 0$ in E2, contour levels = $(8 \times 10^{-3}, -5.34 \times 10^{-2}; 7.85 \times 10^{-3})$, (*c*) $\langle p\rangle\partial\langle v\rangle/\partial y$ at $x = 0$ in E1, contour levels = $(3 \times 10^{-2}, -9.32 \times 10^{-2}, 1.61 \times 10^{-1})$; (*d*) $\langle p\rangle\partial\langle w\rangle/\partial z$ at $x = 0$ in E1, contour levels = $(3 \times 10^{-2}, -9.51 \times 10^{-2}, 1.27 \times 10^{-1})$. (*e*) Schematic of the near-wall intercomponent energy transfer.

is noteworthy that this λ_2-based CS eduction scheme is generally applicable to both free- and wall-bounded turbulent shear flows and is seen to accurately extract fully three-dimensional vortical structures with minimal smearing.

By sampling the entire extent of streamwise vortices, we have revealed a frequently occurring pattern for near-wall CS: an overlapping array of alternating-signed streamwise vortices repeating in x, with individual structures inclined at 9° in the vertical plane and tilted alternately at +4° and −4° in the horizontal plane. Note that hairpin-type vortices are not present in the near-wall region ($y^+ \leqslant 60$) investigated here; this is consistent with their absence in instantaneous λ_2 data and with two-point correlation data of ω_x in (y, z) planes. Some of the instantaneous vortices in the buffer layer are the elongated legs of asymmetric 'arch' or 'horseshoe' vortices extending into the outer region (see, for example, Robinson 1991; Blackburn, Mansour & Cantwell 1996). Since our ensemble-averaged vortices (i.e. λ_2) vanish at $y^+ \approx 50$, the outer portions of these extended vortices are probably smeared out by the ensemble averaging, which is aligned in the buffer layer. Nevertheless, the legs of extended vortices, along with all other near-wall vortices, are the most dynamically significant for skin friction and heat transfer, and hence the focus of our study.

We find that CS tilting in (x, z)-planes due to mutual induction of overlapping vortices is particularly important in generating negative $\overline{p\partial u/\partial x}$, which enables transfer of streamwise fluctuation energy to spanwise and normal components to sustain the CS. This tilting is also responsible for kinked low-speed streaks and internal shear layers with negative $\partial u/\partial x$, both commonly observed but not previously linked to near-wall CS.

We show that a spatial phase difference between u and v within the fully developed structures leads to the dominance of Q4 events over Q2 events near the wall; negative Reynolds stress events (Q1 and Q3 events) were also investigated in the context of CS advection. These effects are readily understood in terms of the phase difference created by the CS's advection of u-fluctuations.

While the results here constitute a snapshot of near-wall CS, the current understanding of the vortex dynamics responsible for their formation and regeneration is far from complete. In this regard, the model of overlapping, alternating-sign streamwise CS presented in this paper as the dominant near-wall structure (figure 10*a,b*) serves as a useful starting point, i.e. initial condition, for further studies of the evolutionary dynamics of near-wall CS. By construction, our eduction technique selects streamwise vortices which are in their active phase of evolution. By initializing DNS with the CS pattern observed, we expect to obtain a 'clean' CS evolution which is amenable to detailed analysis and interpretation (like the approach used by us to study mixing layer transition (see Schoppa, Hussain & Metcalfe 1995)). In contrast to the multitude of irregular structures in the instantaneous field, the flows thus obtained will contain only a few (opposite-signed) vortices whose spatiotemporal evolution can be easily tracked. Since these CS are directly extracted from fully developed turbulent flows, their unconstrained evolution serves as a useful complement to recent results for minimal flow domains.

This research was funded by ONR grant N00014-94-1-0510 and NASA/Ames grant NCA2-317.

REFERENCES

Antonia, R. A. & Bisset, D. K. 1990 Spanwise structure in the near-wall region of a turbulent boundary layer. *J. Fluid Mech.* **210**, 437.

Batchelor, G. K. 1967 *Introduction to Fluid Dynamics*. Cambridge University Press.

Bernard, P. S., Thomas, J. M. & Handler, R. A. 1993 Vortex dynamics and the production of Reynolds stress. *J. Fluid Mech.* **253**, 385.

Blackburn, H. M., Mansour, N. N. & Cantwell, B. J. 1996 Topology of fine-scale motions in turbulent channel flow. *J. Fluid Mech.* **310**, 269.

Blackwelder, R. F. & Eckelman, H. 1979 Streamwise vortices associated with the bursting phenomenon. Part 3. *J. Fluid Mech.* **94**, 577.

Blackwelder, R. F. & Kaplan, R. E. 1976 On the wall structure of the turbulent boundary layer. *J. Fluid Mech.* **76**, 89.

Bogard, D. G. & Tiederman, W. G. 1986 Burst detection with single-point velocity measurement. *J. Fluid Mech.* **162**, 389.

Brooke, J. W. & Hanratty, T. J. 1993 Origin of turbulence-producing eddies in a channel flow. *Phys. Fluids* A **5**, 1011.

Cantwell, B. J. 1981 Organized motion in turbulent flow. *Ann. Rev. Fluid Mech.* **13**, 457.

Chong, M. S., Perry, A. E. & Cantwell, B. J. 1990 A general classification of three-dimensional flow field. *Phys. Fluids* A **2**, 765.

Corino, E. R. & Brodkey, R. S. 1969 A visual investigation of the wall region in turbulent flow. *J. Fluid Mech.* **37**, 1.

Fiedler, H. E. 1988 Coherent structures in turbulent flows. *Prog. Aero. Sci.* **25**, 231.

Hamilton, J. M., Kim, J. & Waleffe, F. 1995 Regeneration mechanisms of near-wall turbulence structures. *J. Fluid Mech.* **287**, 317.

Hayakawa, M. 1992 Vorticity-based conditional sampling for identification of large-scale vortical structures in turbulent shear flows. In *Eddy Structure Identification in Free Turbulent Shear Flows* (ed. J. P. Bonnet & M. N. Glauser), p. 45. Kluwer.

Hunt, J. C. R., Wray, A. A. & Moin, P. 1988 Eddies, stream, and convergence zones in turbulent flows. *Center for Turbulence Research Report CTR*-S88, p. 193.

Husain, H. & Hussain, F. 1993 Elliptic jets. Part 3. Dynamics of preferred mode coherent structure. *J. Fluid Mech.* **248**, 315.

Hussain, A. K. M. F. 1980 Coherent structure and studies of perturbed and unperturbed jets. In *The Role of Coherent Structures in Modelling Turbulence and Mixing* (ed. J. Jimenez), p. 136. Springer.

Hussain, A. K. M. F. 1983*a* Coherent structures — reality and myth. *Phys. Fluids* **26**, 2816.

Hussain, A. K. M. F. 1983*b* Coherent structures and incoherent turbulence. In *Turbulence and Chaotic Phenomena in Fluids.* (ed. T. Tatsumi), p. 453. North-Holland.

Hussain, A. K. M. F. 1986 Coherent structures and turbulence. *J. Fluid Mech.* **173**, 303.

Hussain, A. K. M. F. & Hayakawa, M. 1987 Eduction of large-scale organized structures in a turbulent plane wake. *J. Fluid Mech.* **180**, 193.

Hussain, F., Jeong, J. & Kim, J. 1987 Structure of turbulent shear flows. *Center for Turbulence Research Report CTR*-S87, p. 273.

Hussain, A. K. M. F. & Zaman, K. B. M. Q. 1980 Vortex pairing in a circular jet under controlled excitation, Part 2. Coherent structure dynamics. *J. Fluid Mech.* **101**, 493.

Jeong. J. & Hussain, F. 1992 Coherent structure near the wall in a turbulent channel flow. *Proc. of Fifth Asian Congress of Fluid Mech., Taejon, Korea* (ed. K. S. Chang & H. Choi), p. 1262.

Jeong. J. & Hussain, F. 1995 On the identification of a vortex. *J. Fluid Mech.* **285**, 69.

Jimenez, J. & Moin, P. 1991 The minimal flow unit in near-wall turbulence. *J. Fluid Mech.* **225**, 213.

Johansson, A. V., Alfredsson, P. H. & Kim, J. 1991 Evolution and dynamics of shear-layer structures in near-wall turbulence. *J. Fluid Mech.* **224**, 579.

Kida, S. & Tanaka, M. 1994 Dynamics of vortical structures in a homogeneous shear flow, *J. Fluid Mech.* **274**, 43.

Kim, J. 1989 On the structure of pressure fluctuations in simulated turbulent channel flow. *J. Fluid Mech.* **205**, 421.

Kim, J. & Hussain, F. 1993 Propagation velocity of perturbations in turbulent channel flow. *Phys. Fluids* A **5**, 695.

Kim, J., Moin, P. & Moser, R. D. 1987 Turbulence statistics in fully developed channel flow at low Reynolds number. *J. Fluid Mech.* **177**, 133.

Klebanoff, P. S. 1954 Characteristics of turbulence in a boundary layer with zero pressure gradient. *NACA TN*-3178.

Kline, S. J., Reynolds, W. C., Schraub, F. A. & Rundstadler, P. W. 1967 The structure of turbulent boundary layer. *J. Fluid Mech.* **30**, 741.

Kline, S. J. & Robinson. S. K. 1989 Turbulent boundary layer structure: progress, status and challenges. *Proc. IUTAM Symp. Struct. of Turbulence and Drag Reduction, Zurich.*

Melander, M. V. & Hussain, F. 1994 Core dynamics on a vortex column. *Fluid Dyn. Res.* **13**, 1.

Mumford, J. C. 1982 The structure of large eddies in fully developed turbulent shear flows. Part 2. The plane wake. *J. Fluid Mech.* **137**, 447.

Robinson, S. K. 1991 Coherent motions in the turbulent boundary layer. *Ann. Rev. Fluid Mech.* **23**, 601.

Schoppa, W. 1997 PhD dissertation, University of Houston (in preparation).

Schoppa, W., Hussain, F. & Metcalfe, R. W. 1995 A new mechanism of small-scale transition in a plane mixing layer: core dynamics of spanwise vortices. *J. Fluid Mech.* **298**, 23.

Spalart, P. R. 1988 Direct simulation of a turbulent boundary layer up to $R_\theta = 1410$. *J. Fluid Mech.* **187**, 61.

Stretch, D. 1989 Patterns in simulated turbulent channel flow. *Center for Turbulence Research Report CTR*-S89, p. 261.

Swearingen, J. D. & Blackwelder, R. F. 1987 The growth and breakdown of streamwise vortices in the presence of a wall. *J. Fluid Mech.* **182**, 225.

Tennekes, T. & Lumley, J. L. 1972 *A First Course in Turbulence*. MIT Press.

Townsend, A. A. 1979 Flow patterns of large eddies in a wake and in a boundary layers. *J. Fluid Mech.* **95**, 515.

Willmarth, W. W. & Lu, S. S. 1972 Structure of the Reynolds stress near the wall. *J. Fluid Mech.* **55**, 65.